

## Chapter 3

# Study on hole impurity triggered magnetism in Fe doped $(\text{Te})_{1-x}\text{Sb}_x$ bulk alloys

### 3.1 Introduction

The past studies on dilute magnetic semiconductors mainly focused on evaluating oxide-based, II-IV group and III-V group of semiconductors under different conditions of sample preparation. In addition, investigations on the type of dopant material to be added was also on the spotlight which would help enhance the Curie temperature  $T_C$  of the materials beyond room temperature. Elemental semiconductors, on the other hand like Si, Ge, Se, Te, etc. having lower band gap values, have not received much attention in terms of investigating their likelihood to function as a potential dilute magnetic semiconductor.

Tellurium is one such elemental semiconductor that, till recently, has been widely explored to understand their optical, thermoelectric, and biological applications [1]. In the past, studies on elemental Germanium to probe its applicability as a dilute magnetic semiconductor was undertaken [2-5]. Tellurium is a metalloid and tellurides (salts of  $\text{Te}^{2-}$  that are formed with elements belonging to group IA, IIA and lanthanides) are the most stable compounds of tellurium. Trigonal Te having space group  $P3_121$  is found to undergo a transition under shear strain to a topological insulator phase [6]. Tellurium's comparatively large atomic mass and complex crystal structure, when compared to semiconductors of group IV and III-V that are well studied, should result in a substantially lower lattice thermal conductivity [7]. Tellurium has a band gap of  $\sim 0.32$  eV which makes it suitable as photoconductors, field effect transistors, cooling devices, etc. [8-11]. Ultrathin Te nanowire films exhibit reversibly switched photoelectric characteristics in their mesostructures and the number of mesostructured

nanowire monolayers as well as the light intensity influences the photocurrent [8]. In bulk tellurium, as a result of circular polarized light, photogalvanic effect was found to be induced [12]. Ultrathin trigonal tellurium (t-Te) produced through high-yield solution-processing was introduced as a novel piezoelectric nanomaterial. Only the strain created in its radial direction, wherein it has an asymmetric crystal structure, could activate it piezoelectrically [13]. It has been found that tellurium in nanoscale form exhibits special physical characteristics with relation to their band gaps and their potential utility for treating bacterial illnesses [14, 15]. In p-type Te bulk samples that were investigated in the mid-infrared spectral range, tellurium vacancies in them presented a hole density level to exceed  $10^{14} \text{ cm}^{-3}$  [16]. Tellurium thin films were found to have exceptional nonlinear optical absorption properties and in the visible range, it could be a viable optical modulator [17]. Currently, work on 2-dimensional tellurium has gained momentum to accelerate development of next-generation electronic and optoelectronic devices by making use of optimized growth techniques [18, 19]. Elemental tellurium, having semiconducting nature, was found to have a figure of merit  $zT$  of around 1.0 and it has bridged the high-performance gap between 300 K and 700 K for elemental thermoelectrics [20]. On application of 4 GPa hydrostatic pressure, a structural phase transition from the trigonal to Te II structure was seen, accompanied with a decrease in resistivity. The Te II phase exhibits metallic characteristics, whereas the semiconducting feature is present up until the phase change [21]. The Te band's non-centrosymmetric crystal structure and robust spin-orbit interaction has reignited interest in its topological character [22, 23]. A changeover in topological phase of elemental semiconductor from being a semiconductor to being a Weyl semimetal has been observed as an effect of pressure [24]. Tellurium Weyl semiconductor thin flakes was seen to exhibit a negative magnetoresistance in a parallel magnetic field over a broad temperature range [25]. However, quantum linear magnetoresistance has also been observed under pulsed magnetic field measurement up to 57 T in high-

mobility elemental tellurium [26]. In silicon doped tellurium, which is a non-oxide and non-nitride based semiconductor, room temperature ferromagnetism was demonstrated which was a first of its kind [27]. Magnetization has also been observed in elemental tellurium which has been induced due to current that contributes to spin-splitting of the bulk band [28].

In the present chapter, for the enhancement of magnetic properties of elemental semiconductor tellurium, it is doped with dilute quantity of Fe which acts as a hole dopant. The amount of magnetic ion Fe is kept at 0.05 for developing a dilute magnetic semiconductor so that no Fe clusters or undesirable magnetic phases are formed that might result in magnetization. Additionally, there were studies on hole doping that aids in an indirect exchange mechanism between the magnetic ions that feeds ferromagnetism in the system [29]. Hence to see the effect of hole doping, substitution of Sb, a group V element, is made into tellurium which releases further holes into the system. By utilizing various characterization methodologies, as detailed in the following sections, their properties are studied.

### **3.2 Experimental Procedure**

To prepare bulk powder samples of  $\text{Fe}_{0.05}(\text{Te})_{1-x}\text{Sb}_x$  where  $x = 0, 0.01, 0.03$  and  $0.05$ , desired quantities of Te, Fe and Sb (Alfa Aesar, 99.999% pure) are measured and transferred to quartz ampoules. These ampoules were vacuum-sealed in a rotary pump under the pressure of  $>10^{-5}$  Torr. The sealed ampoules were heated repeatedly using an oxy-butane flame to attain the appropriate temperatures for the melting of the powders. After all the powder samples blended in well, the temperature of the ampoules was brought down by immediately dropping them in a container filled with icy water. This prompted the formation of solidified ingots which were grinded and then studied.

Structural aspects of the sample were studied using Bruker D8 Advance X-ray Diffractometer (XRD) having  $\text{CuK}_\alpha$  radiation of wavelength  $1.5406 \text{ \AA}$  in the

range of 20° to 70°. Using Fourier Transform Infrared Spectroscopy (Shimadzu FTIR – 8400 S), band gap values were calculated. Using Quantum Design's Physical Property Measurement System (PPMS), measurements of temperature and magnetic field dependent electrical resistivity and magnetic resistivity were made. Magnetic measurements including DC and AC were carried out using Quantum design make Superconducting Quantum Interface Device – Vibrating Sample Magnetometer (SQUID-VSM) magnetometer equipped with Pulse Tube Cooler in the temperature range 10 K – 300 K and magnetic field range of up to 7T.

### **3.3 Results and Discussion**

#### **3.3.1 Structural Studies**

Structural characterization of  $\text{Fe}_{0.05}(\text{Te})_{1-x}\text{Sb}_x$  bulk alloys is done using X-ray Diffractometer (XRD) and the diffraction patterns are shown in Fig. 3.1. The peaks observed in the diffraction pattern are positioned at the (hkl) plane values of (100), (101), (102), (110), (111), (003), (201), (202), (113), (211) and (114). These peaks are found to exactly correspond to that of elemental Tellurium which has a hexagonal structure with space group  $P3_121$  (JCPDF 36-1452). No presence of any secondary phases is found in the samples. The Te matrix has incorporation of Fe and Sb, which is validated by a minor shift in peak positions while maintaining the crystal structure. Using the XRD data and plane spacing equation for the hexagonal structure, the lattice parameters of the samples are calculated [30]. We can also estimate crystallite size (D) values from the Scherrer's formula which considers the crystallite size to be solely responsible for broadening of peaks.

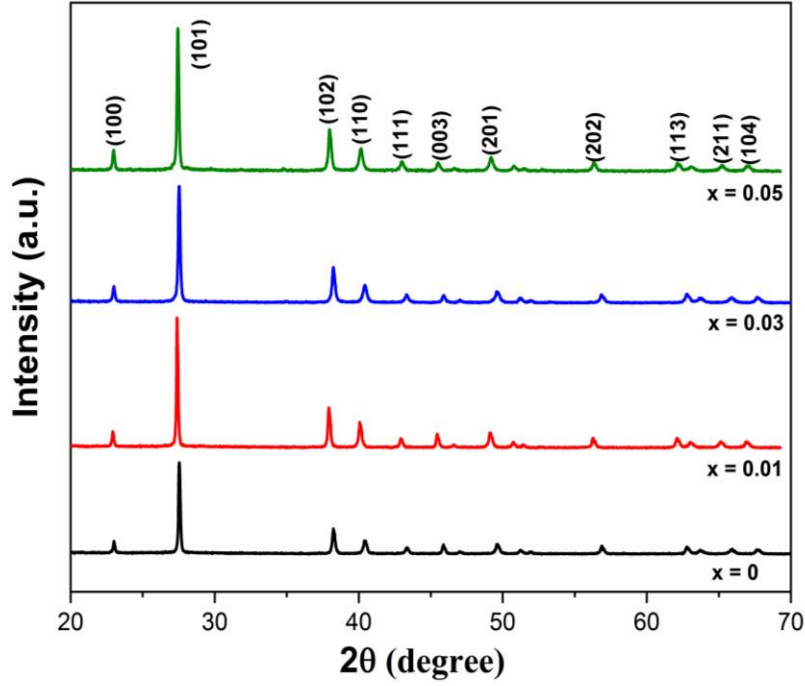


**Figure 3.1:** XRD diffraction pattern of  $Fe_{0.05}(Te)_{1-x}Sb_x$  bulk alloys for  $x = 0, 0.01, 0.03$  and  $0.05$ .

There can also be factors other than crystallite size that could be responsible for peak broadening. The process of doping can give rise to strain and defects in the lattice which can also contribute to the broadening of peaks, and this is explained using Williamson – Hall (W-H) plot and Size – Strain plot (SSP) [31]. They are expressed by the equations 3.1 and 3.2 respectively. These analyzing techniques consider peak broadening to be the combined effect of size and strain induced effects.

$$\beta \cdot \cos\theta = \frac{0.9\lambda}{L} + 4\varepsilon \cdot \sin\theta \quad (3.1)$$

$$(d_{hkl} \cdot \beta_{hkl} \cdot \cos\theta)^2 = \frac{k\lambda}{L} \cdot (d_{hkl}^2 \cdot \beta_{hkl} \cdot \cos\theta) + \frac{\varepsilon^2}{4} \quad (3.2)$$

Here  $L$  denotes the crystallite size,  $\theta$  the Bragg's angle,  $\lambda$  the wavelength of the XRD source i.e.  $CuK_{\alpha}$ ,  $\beta$  represents full width at half maximum (FWHM) of the corresponding peaks,  $\varepsilon$  the strain in the lattice and  $d_{hkl}$  the distance between the adjoining planes. In SSP technique, the XRD profile is considered to be composed of Lorentzian and Gaussian function wherein the size broadened

profile is depicted as Lorentzian function and the strain broadened profile as Gaussian function. Additionally, reflections occurring at higher angles are given less importance in SSP method due to less precision. Figure 3.2 and Fig. 3.3 illustrates the plot of W-H and SSP analysis respectively. From the slope and intercept of  $(4 \cdot \sin\theta$  vs  $\beta \cdot \cos\theta$ ), the value of lattice strain and crystallite size can be inferred whereas the slope and intercept of  $(d_{hkl}^2 \cdot \beta_{hkl} \cdot \cos\theta)$  vs  $(d_{hkl} \cdot \beta_{hkl} \cdot \cos\theta)^2$  plot gives the crystallite size and strain values respectively. The values of the above parameters are listed out in Table 3.1. The smaller values of crystallite size obtained from Scherrer's equation is because of the disparity in how the particle size distribution is averaged. From the broadening analysis, a good correlation between the values of crystallite size obtained from W-H plot and SSP plot can be seen. Also, lattice strain from SSP plot is greater than that from W-H plot as SSP method takes into consideration the peak shape difference which is not the case in W-H method.

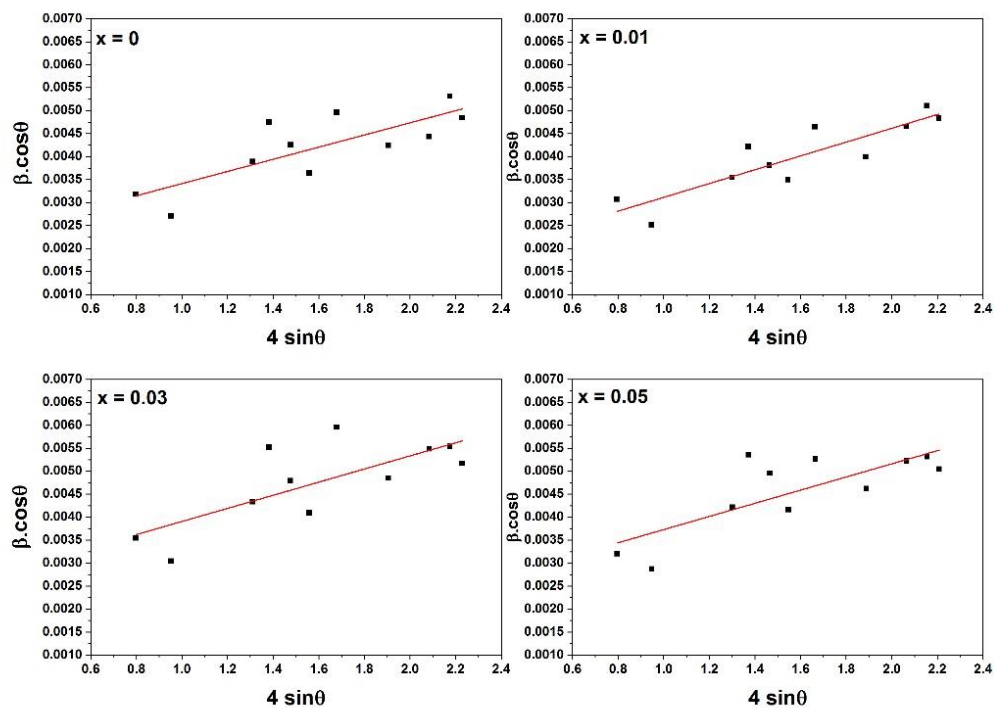


**Figure 3.2:** Plot of Williamson-Hall analysis of  $Fe_{0.05}(Te)_{1-x}Sb_x$  bulk alloys. Linear fit to the data is represented by the red line.

**Table 3.1:** Structural parameters of  $Fe_{0.05}(Te)_{1-x}Sb_x$  calculated from XRD data.

Samples	From XRD		Crystallite Size (nm)			Lattice Strain	
	a (Å)	c (Å)	Scherrer	W-H	SSP	W-H	SSP
$Fe_{0.05}(Te)$	4.457	5.928	34.279	47.977	51.164	0.0013	0.0122
$Fe_{0.05}(Te)_{0.99}Sb_{0.01}$	4.493	5.979	36.246	54.803	55.684	0.0015	0.0118
$Fe_{0.05}(Te)_{0.97}Sb_{0.03}$	4.493	5.944	30.341	41.513	45.312	0.0014	0.0135
$Fe_{0.05}(Te)_{0.95}Sb_{0.05}$	4.488	5.974	31.667	44.017	50.975	0.0014	0.0136

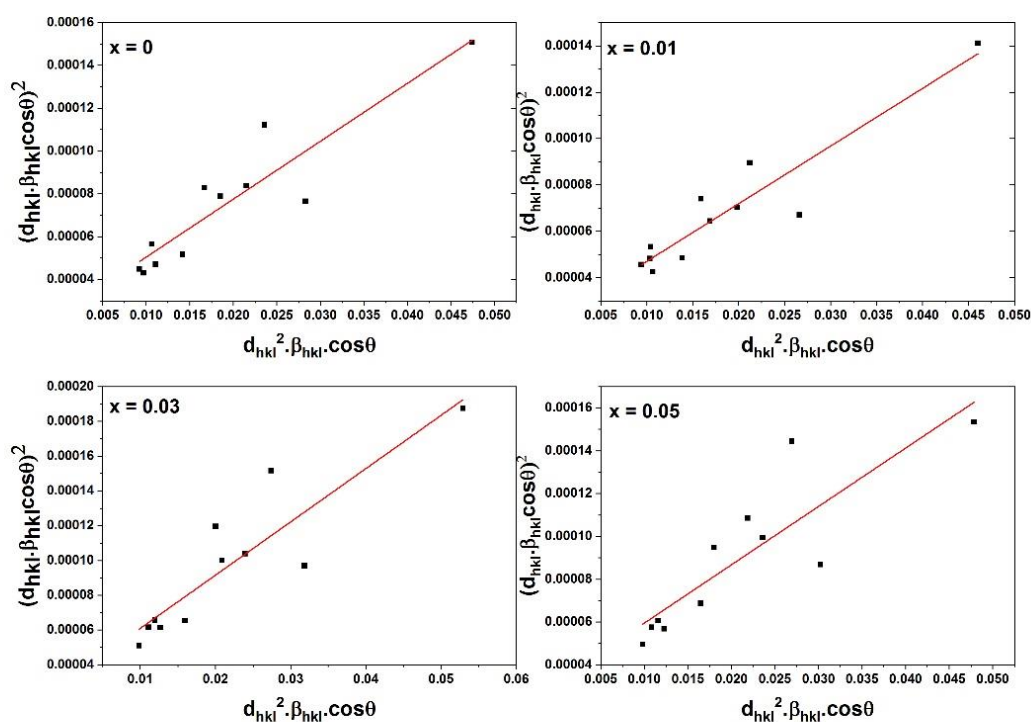


**Figure 3.3:** Size-Strain plot with linear fit to the points of  $Fe_{0.05}(Te)_{1-x}Sb_x$  samples as indicated by red line.

### 3.3.2 FTIR Studies

In Fig. 3.4, FTIR spectra of  $Fe_{0.05}(Te)_{1-x}Sb_x$  ( $x = 0, 0.01, 0.03$  and  $0.05$ ) bulk samples are presented. The range of wavenumber in which the measurements were carried out for recording the spectra is from  $500 - 3500 \text{ cm}^{-1}$

<sup>1</sup>. The signature bands of Tellurium are marked in the figure as inferred from literature [32]. In the present study, since Te is doped with dilute quantity of Fe, the effects of doping with Fe leads to the formation of two vibrational peaks between 2800 cm<sup>-1</sup> and 3000 cm<sup>-1</sup>. Furthermore, two additional bands, one at 850 cm<sup>-1</sup> and the other at 980 cm<sup>-1</sup> are also observed on the substitution of Sb into the system. These bands could have their origins from the bond formation between Te and Sb.

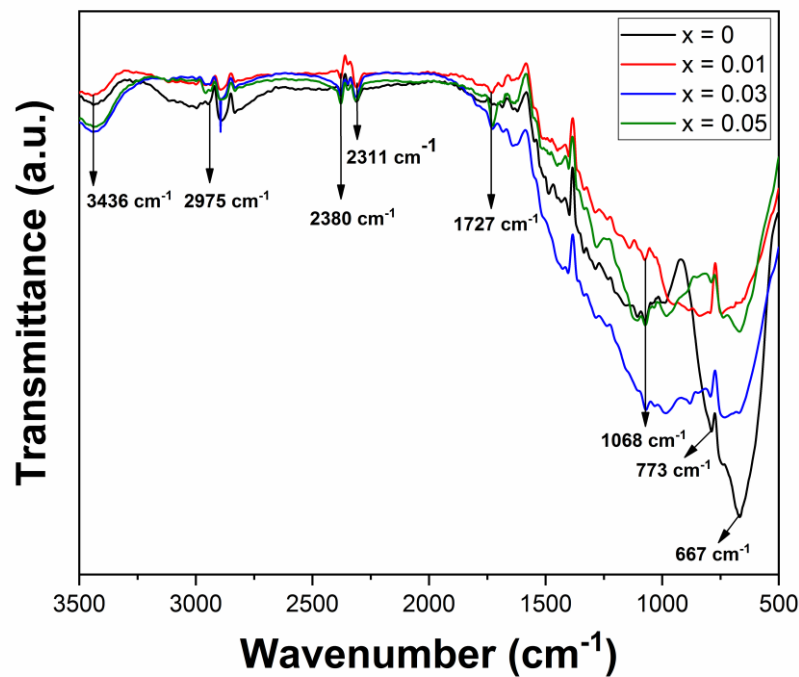


**Figure 3.4:** FTIR spectra of  $Fe_{0.05}(Te)_{1-x}Sb_x$  bulk alloys for  $x = 0, 0.01, 0.03$  and  $0.05$  marked with signature peaks of Tellurium.

The peak information from the FTIR spectra is also used for deducing the band gap of those semiconductors whose band gap value falls in the IR region. This is accomplished using the formula given below.

$$(\alpha h\nu) = A(h\nu - E_g)^n \quad (3.3)$$

where  $\alpha$ ,  $A$  and  $E_g$  denotes co-efficient of absorption, a constant and band gap of the corresponding sample respectively. Since the spectra is recorded in the transmittance mode, the value of constant  $A$  is derived from the transmittance intensity.

In order to derive the band gap values, linear region of the plot  $(\alpha hv)^{1/n}$  vs  $hv$  is projected onto the X-axis by extrapolating it. Since tellurium has direct band gap energy, the value of  $n$  is assumed to be  $1/2$  and the plots are shown in Fig. 3.5. From the literature survey, the band gap of bulk tellurium is found to be  $\sim 0.32$  eV [33]. However, doping with Fe reduces the value to 0.20 eV. A band level formation within the band gap of Te due to doping of Fe = 0.05 could be the reason for such a dramatic decrease. With introduction of Sb into the system, the band gap value is seen to remain almost same within the experimental error  $\sim 0.21$  eV for  $x = 0.01$  sample. Further increase in the concentration of Sb also has no effect on the band gap for  $x = 0.03$  and  $x = 0.05$  samples. Thus, although Sb brings in holes into the system the effect of holes does not result in any change in the band gap values of Te. The values of band gap and the corresponding values of error obtained from the linear fit of the plot are listed in Table 3.2.

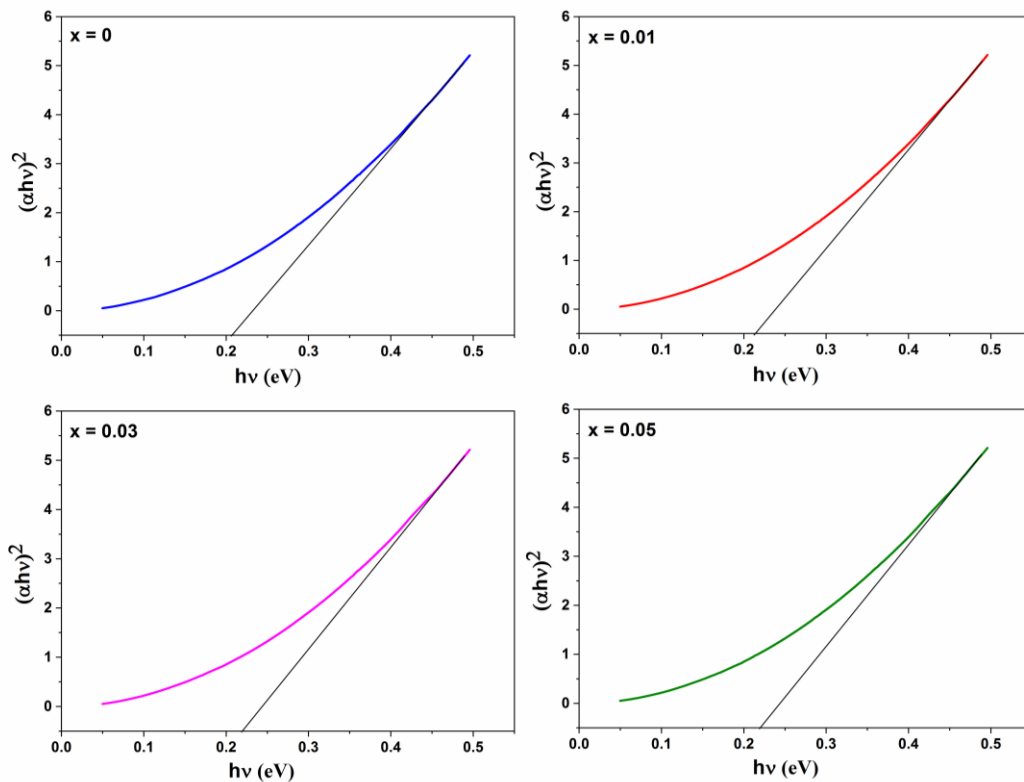


**Figure 3.5:** Plots of  $(\alpha hv)^2$  vs. energy  $hv$  to find band gap of  $Fe_{0.05}(Te)_{1-x}Sb_x$  bulk alloys.

**Table 3.2:** Band gap values of  $Fe_{0.05}(Te)_{1-x}Sb_x$  samples along with the corresponding error.

Samples	Direct Band Gap
	eV
$Fe_{0.05}(Te)$	$0.20 \pm 0.02$
$Fe_{0.05}(Te)_{0.99}Sb_{0.01}$	$0.21 \pm 0.02$
$Fe_{0.05}(Te)_{0.97}Sb_{0.03}$	$0.22 \pm 0.02$
$Fe_{0.05}(Te)_{0.95}Sb_{0.05}$	$0.22 \pm 0.02$

### 3.3.3 Electrical Studies

Using Physical Property Measurement System (PPMS), the resistivity measurement as a function of temperature was performed in the range 2 K – 300 K. Initial data is collected in zero field, only to later subject the samples to external magnetic fields of 5 T and 8 T and see whether this would result in any difference in the resistivity values. The plots shown in Fig. 3.6(a-d) show a similar trend even in the presence of magnetic field.

Tellurium, despite being an elemental semiconductor, also behaves as a semi-metallic, i.e. it comprises features of both, a metal as well as a semiconductor [34]. On analysing the resistivity data of the samples, a negative trend of temperature coefficient of resistivity (TCR) is observed. Thus, the samples can be termed as semiconducting and even application of magnetic field does not bring any change in its property. Localization effects of charge carriers is what seems to be the cause this semiconducting behaviour to occur [35]. The low temperature resistivity curve of samples  $x = 0, 0.01$  and  $0.03$  shows an upturn in the value below 25 K. This sharp rise demonstrates the presence of an insulating state in these samples. On the other hand, such a behaviour is absent in  $x = 0.05$  sample which is purely semiconducting in nature. In this sample, a rapid decrease in the resistivity value is also observed in comparison to the other three

samples, as the hole concentration is found to enhance due to increase in the concentration of Sb. A similar tendency of decrease in electrical resistivity with the rise in dopant concentration is also noted in the literature [36].

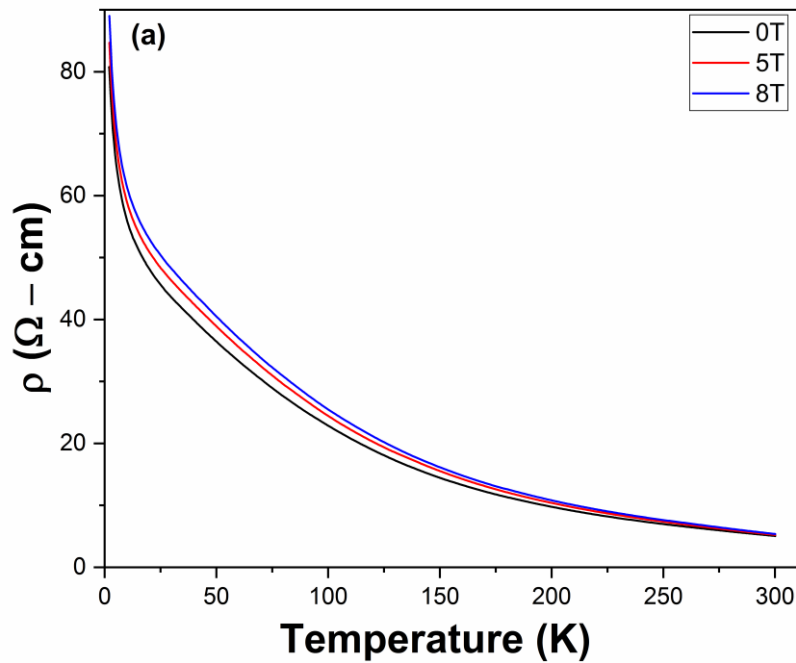


**Figure 3.6(a):** DC electrical resistivity of  $Fe_{0.05}(Te)_{1-x}Sb_x$  bulk alloy for  $x = 0$  at 0T, 5T and 8T.

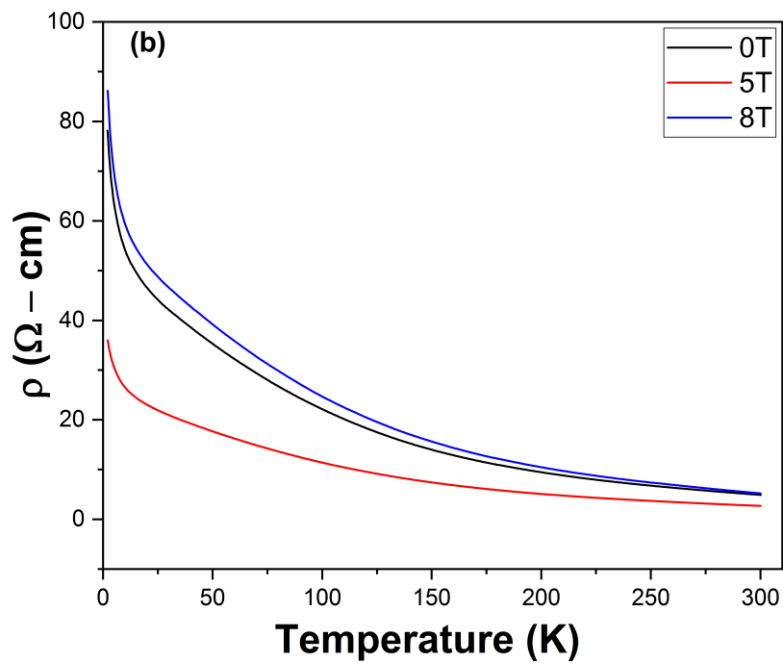


**Figure 3.6(b):** DC electrical resistivity of  $Fe_{0.05}(Te)_{1-x}Sb_x$  bulk alloy for  $x = 0.01$  at 0T, 5T and 8T.

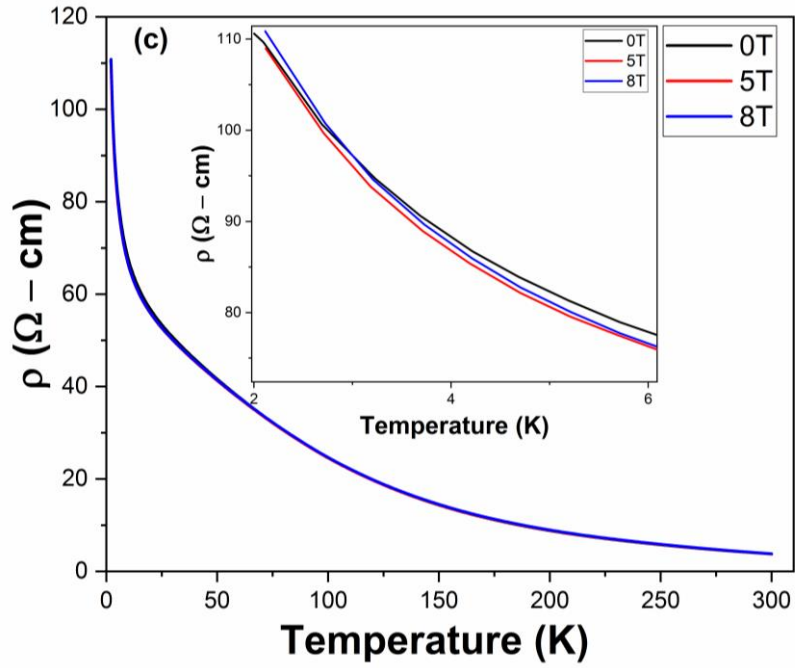


**Figure 3.6(c):** DC electrical resistivity of  $Fe_{0.05}(Te)_{1-x}Sb_x$  bulk alloy for  $x = 0.03$  at 0T, 5T and 8T. Magnified view of the plot is shown in the inset.

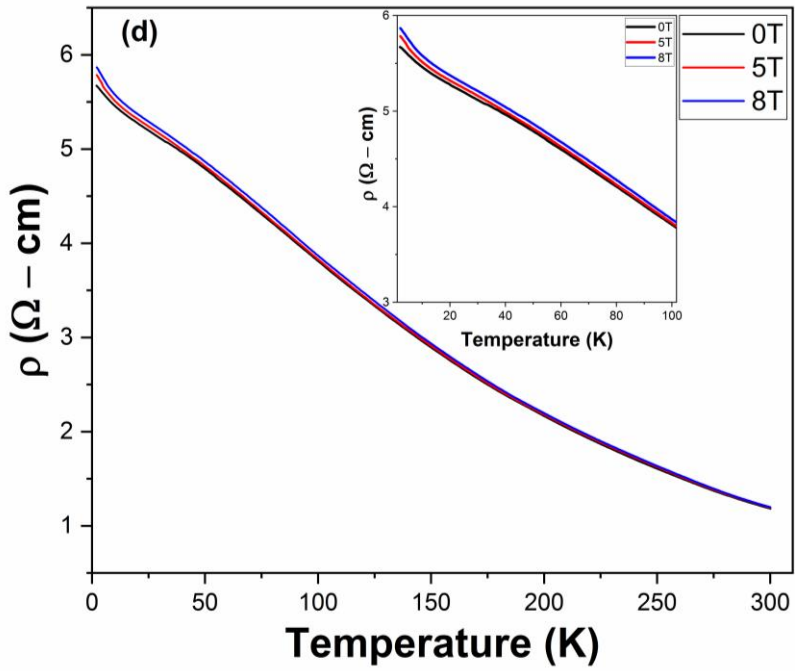


**Figure 3.6(d):** DC electrical resistivity of  $Fe_{0.05}(Te)_{1-x}Sb_x$  bulk alloy for  $x = 0.05$  at 0T, 5T and 8T. Magnified view of the plot is shown in the inset.

Temperature coefficient of resistance alone cannot be counted as the primary distinguishing criteria to determine the conduction regime. The plot of

reduced activation energy which is defined below is also employed to validate the semiconducting nature of the samples [37, 38].

$$W = -[d \ln \rho(T)/d \ln T] \quad (3.4)$$

The W-T plots as seen in Fig. 3.7(a-d) shows a decreasing trend with increasing temperature corresponding to negative value of the slope which thereby confirms a semiconducting conduction regime of the samples.

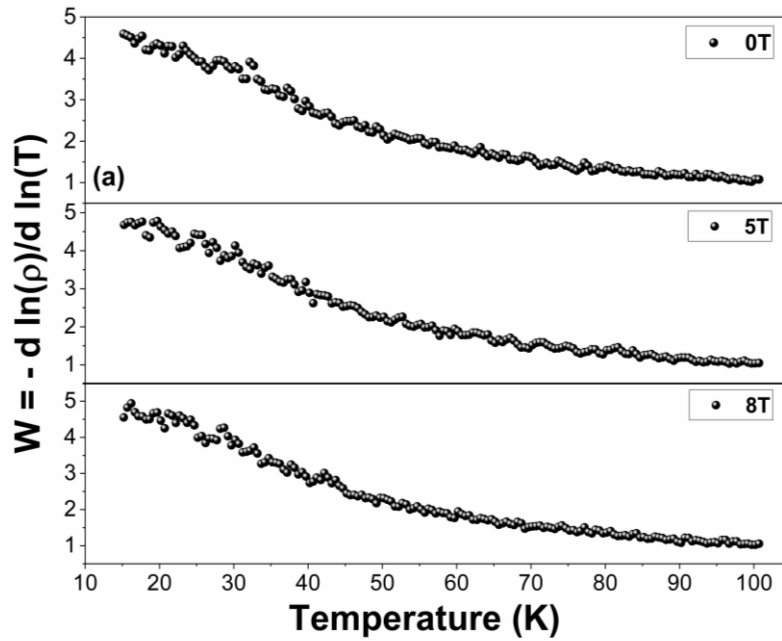


Figure 3.7(a): W-T plot of reduced activation energy for  $x = 0$  sample.

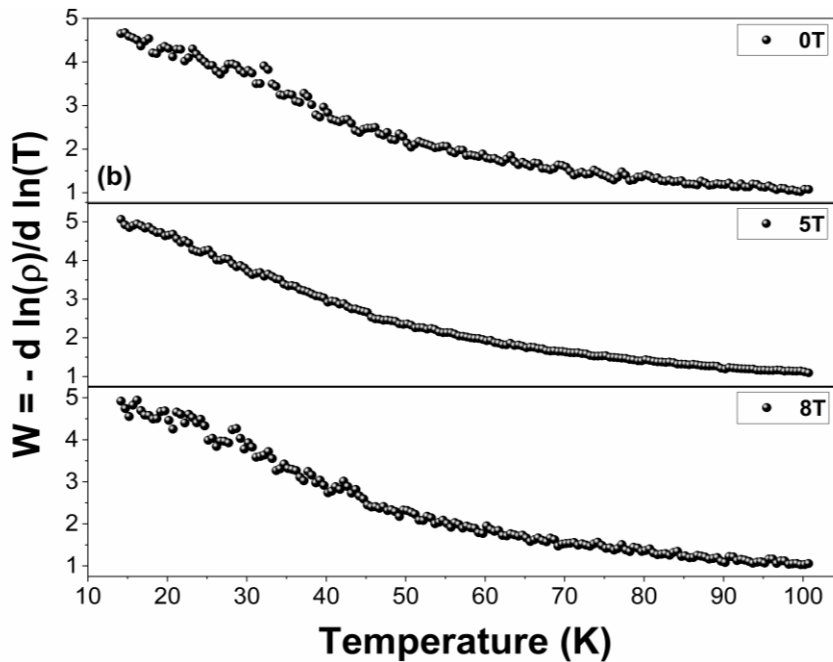


Figure 3.7(b): W-T plot of reduced activation energy for  $x = 0.01$  sample.

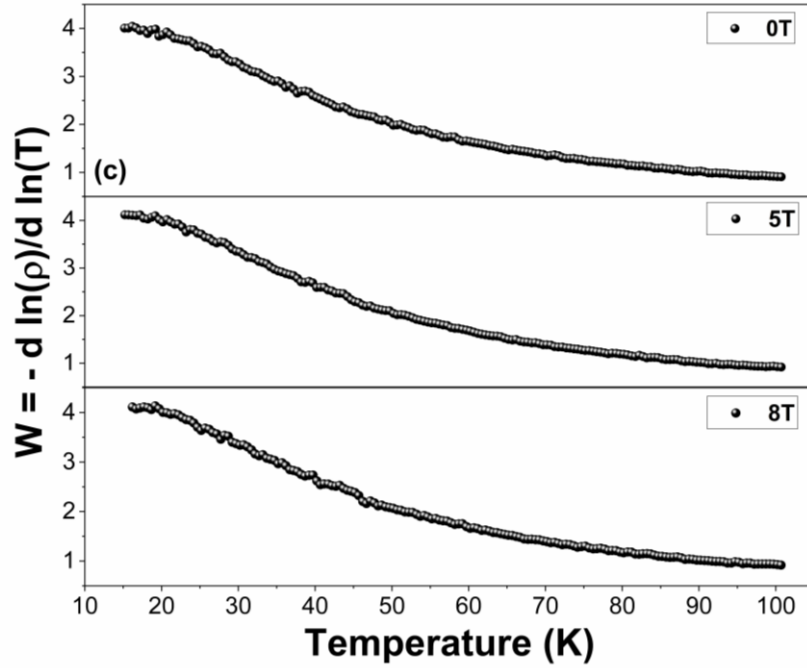


Figure 3.7(c):  $W$ - $T$  plot of reduced activation energy for  $x = 0.03$  sample.

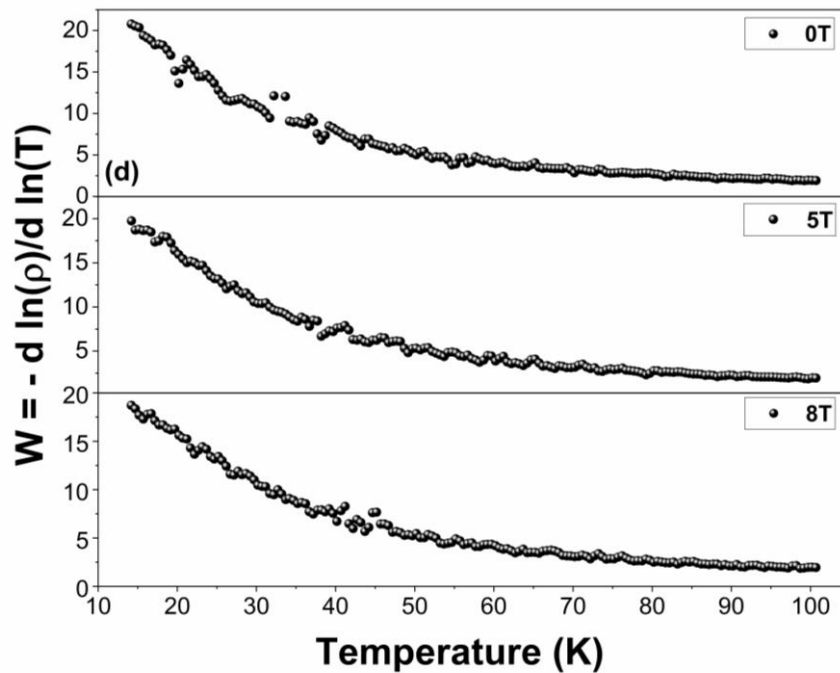


Figure 3.7(d):  $W$ - $T$  plot of reduced activation energy for  $x = 0.05$  sample.

Using different models like small polaron hopping (SPH) model, thermal activation energy model, variable range hopping (VRH) model, the transport properties of the prepared samples with varying concentrations of Sb at  $x = 0$ , 0.01, 0.03 and 0.05 have been explained on the basis of which model is the best

fit to the resistivity data. In the high temperature region, SPH model is found to be dominant as initiation of hopping of small polarons, which are deeply trapped electrons, to their neighbouring sites can be achieved merely through thermal energy. The model is represented by the equation as given below [39].

$$\rho = \rho_0 T \exp(E_a/k_B T) \quad (3.5)$$

where  $\rho_0$  is residual resistivity,  $E_a$  is activation energy,  $k_B$  is Boltzmann constant. SPH model came across as an absolute fit to explain the conductivity mechanism in the high temperature region. From the plots of  $\ln(\rho/T)$  v/s  $T^{-1}$  shown in Fig. 3.8(a-d), a linear fit is made to the linear region in the high temperature range of 255 K – 300 K and from the slope of the fit, activation energy  $E_a$  values are obtained that would initiate the hopping conduction.

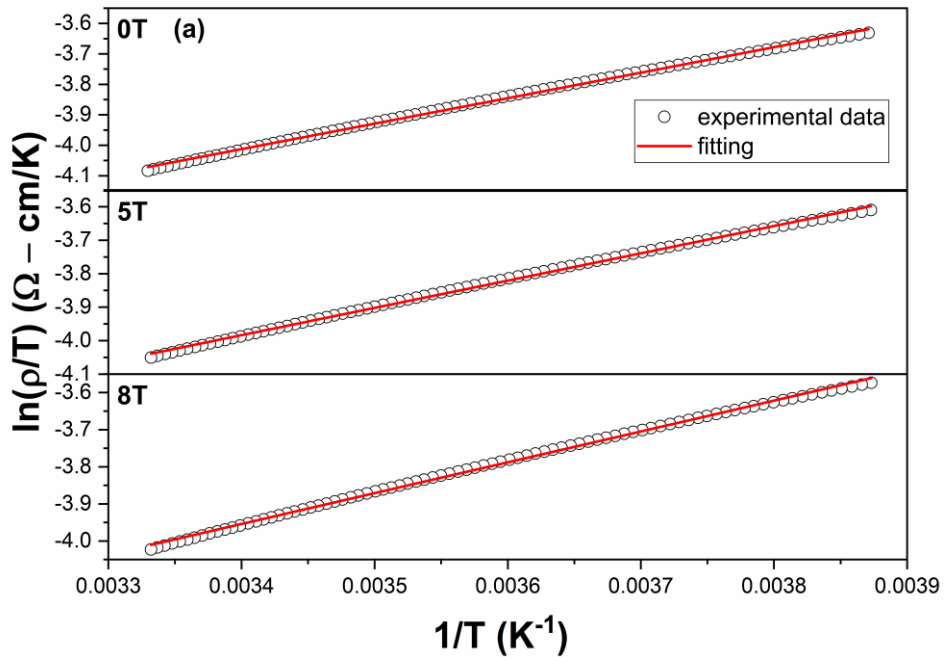


**Figure 3.8(a):** Fitting of SPH model in the high temperature region from 255 K – 300 K of  $x = 0$  sample.

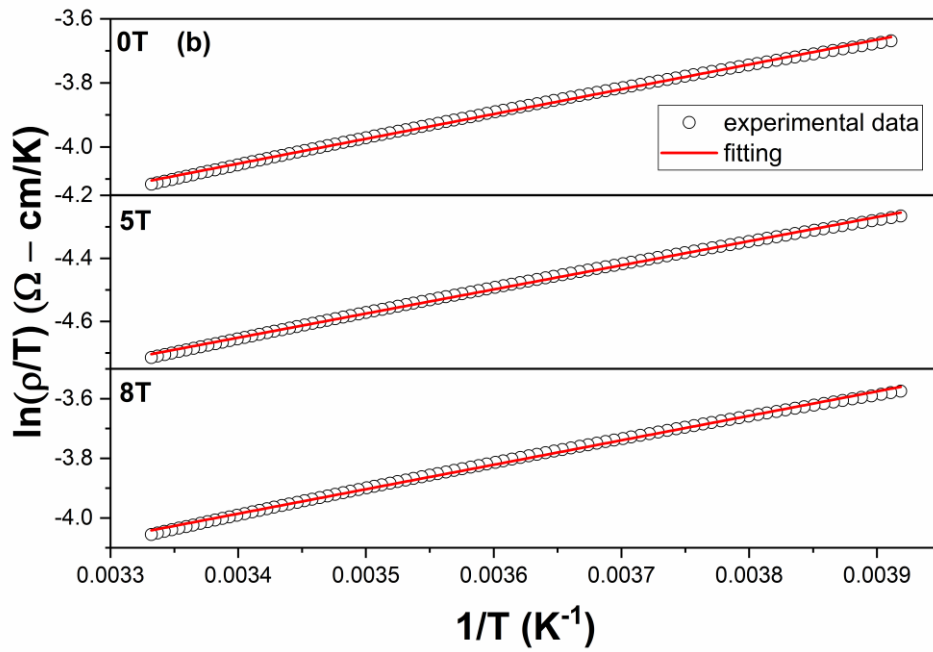


*Figure 3.8(b): Fitting of SPH model in the high temperature region from 255 K – 300 K of  $x = 0.01$  sample.*

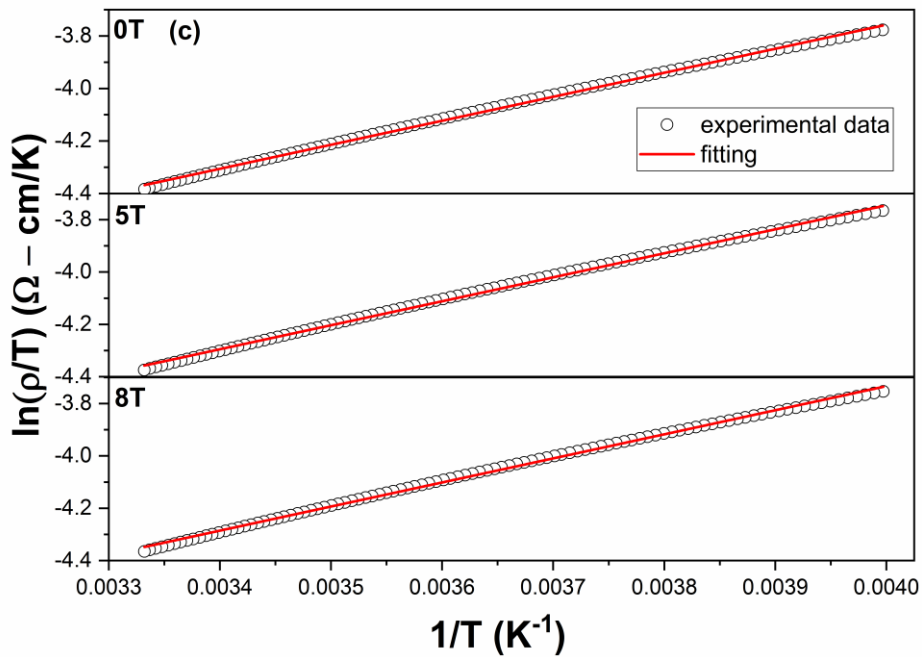


*Figure 3.8(c): Fitting of SPH model in the high temperature region from 255 K – 300 K of  $x = 0.03$  sample.*

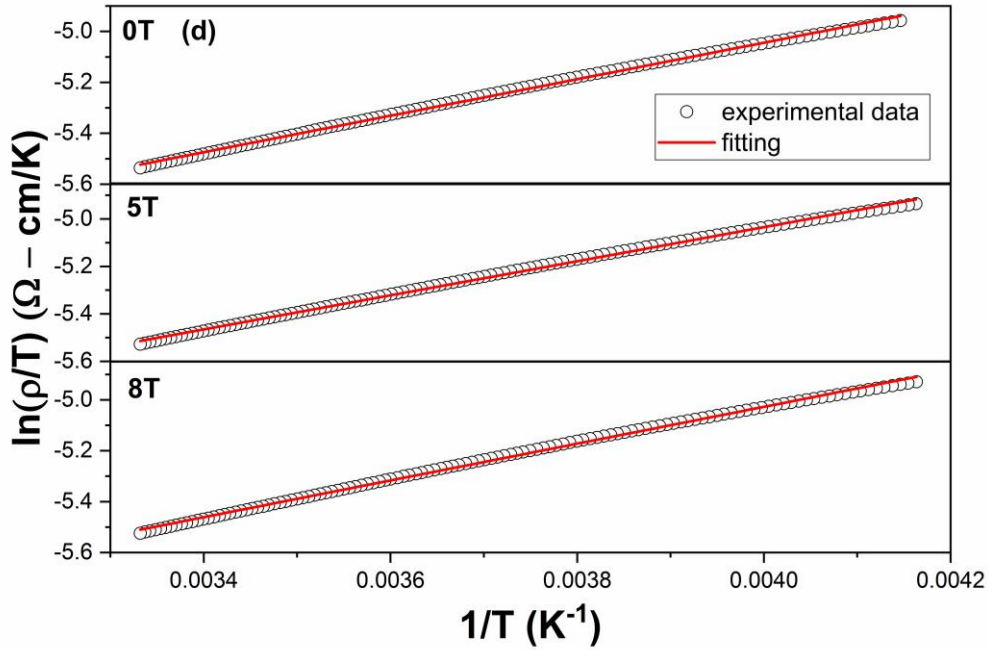


**Figure 3.8(d):** Fitting of SPH model in the high temperature region from 255 K – 300 K of  $x = 0.05$  sample.

**Table 3.3:** Values of Activation energy ( $E_a$ ) in the high temperature region from SPH model fitting.

Samples	$E_a$ values (meV)		
	Applied Magnetic Field		
	0T	5T	8T
$\text{Fe}_{0.05}(\text{Te})$	66.78	66.11	65.67
$\text{Fe}_{0.05}(\text{Te})_{0.99}\text{Sb}_{0.01}$	66.65	65.97	65.30
$\text{Fe}_{0.05}(\text{Te})_{0.97}\text{Sb}_{0.03}$	77.38	76.71	76.40
$\text{Fe}_{0.05}(\text{Te})_{0.95}\text{Sb}_{0.05}$	62.61	61.87	61.39

Table 3.3 provides the values of  $E_a$  which undergoes a decreasing trend for the samples as the magnetic field is increased. Delocalization of charge carriers causes strong charge transfer at high temperatures which is responsible for this decrease in  $E_a$  values [40]. The value of activation energy  $E_a$  is seen to be maximum for  $x = 0.03$  dropping again for  $x = 0.05$ . It seems that there is an

optimum concentration of hole ( $x = 0.03$ ) where the polarons are assumed to be deeply trapped in states that are localized in the forbidden band. As a result, more amount of energy is required for the hopping mechanism to commence and participate in the conduction process.

The temperature dependent resistivity of the samples cannot only be explained by the SPH model in the whole range of temperature. The competence of both 2-D and 3-D VRH model to accurately address the transport mechanism at lower temperatures is put to the test. Unlike in SPH model, thermal energy is not sufficient to activate the hopping process in VRH mechanism. As a result, the electrons look out for a site having lower energy difference thereby initiating the hopping process. Because the hopping range can vary, it is referred to as variable range hopping [41, 42]. As 2-D VRH model is found incompatible in fitting the data points, it is shelved. The expression below represents 3-D VRH model.

$$\rho(T) = \rho_0 \exp(T_0/T)^{1/4} \quad (3.6)$$

where  $\rho_0$  and  $T_0$  indicate Mott parameters.  $T_0$  can be evaluated using the formula  $\frac{3}{2}K_B\alpha^3N(E_F)$  where  $N(E_F)$  corresponds to the density of states having energy equivalent to Fermi energy. The validity of VRH model can be confirmed by plotting  $\ln(\rho)$  v/s  $1/T^{1/4}$ . A linear fit to the data shows that VRH model holds valid in two regions of the plot; one from 150 K – 255 K and other in the range 2 K – 25 K for  $x = 0, 0.01$  and  $0.03$  samples as seen in Fig. 3.9(a-c) and 3.10(a-c). This is not the case with  $x = 0.05$  sample where VRH model is found to be active only in the range 145 K – 195 K. At lower range of temperatures in  $x = 0.05$  sample, it can be assumed that the transport property is not just limited to VRH mechanism but there could also be some other mechanism involved. Hence the VRH model can't be fitted in the low temperature ranges. The plot is shown in Fig. 3.10(d). The value of slope of the linear fit corresponds to the value of Mott's temperature  $T_0$  which in turn corresponds to average energy required for charge

carriers to hop to their neighbouring site. From Table 3.4,  $T_0$  values are seen to decrease with increasing magnetic field. Such a decreasing trend is suggestive of an increase in the density of states  $N(E_F)$  at the Fermi level thereby enhancing the hopping of charge carriers.

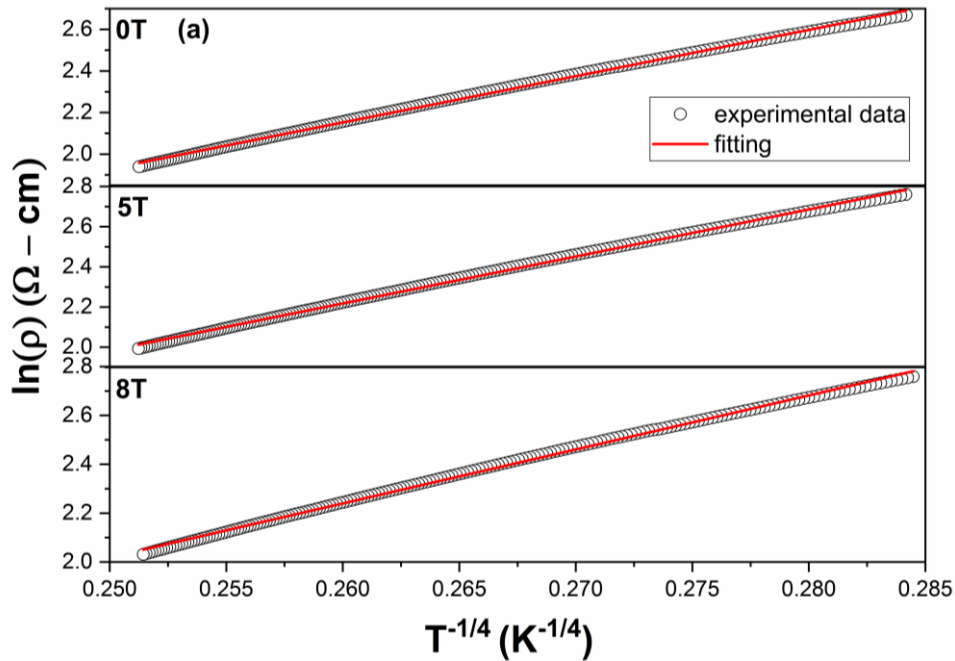


*Figure 3.9(a): Fitting of VRH model in the temperature region from 150 K – 255 K of  $x = 0$  sample.*

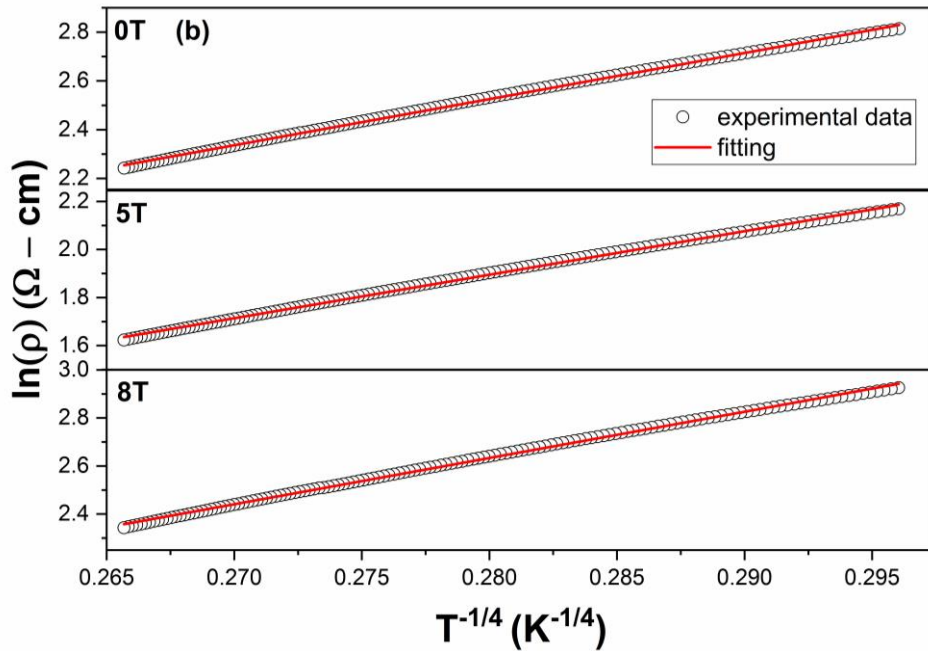


*Figure 3.9(b): Fitting of VRH model in the temperature region from 150 K – 255 K of  $x = 0.01$  sample.*

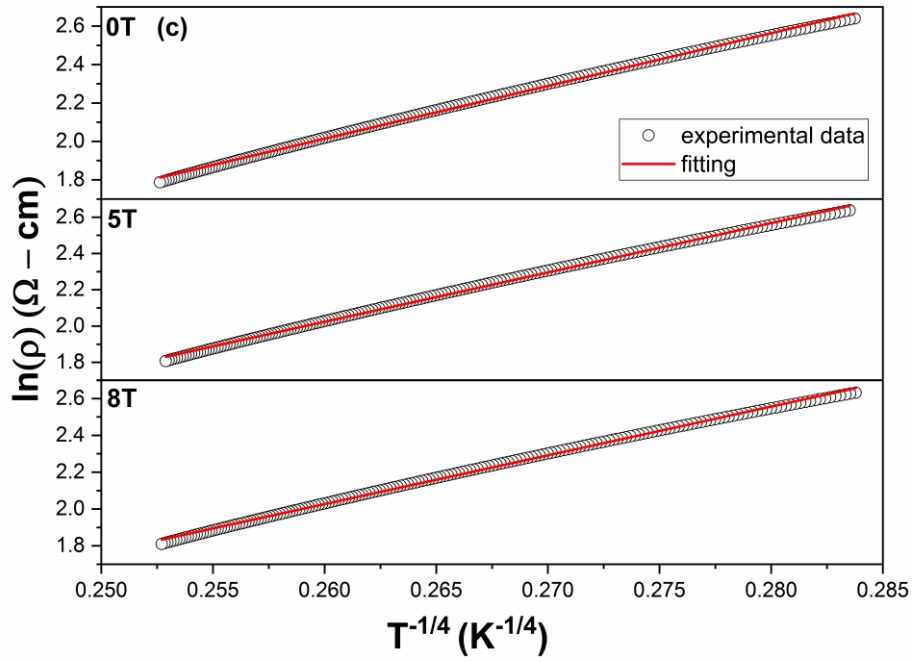


Figure 3.9(c): Fitting of VRH model in the temperature region from 150 K – 255 K of  $x = 0.03$  sample.

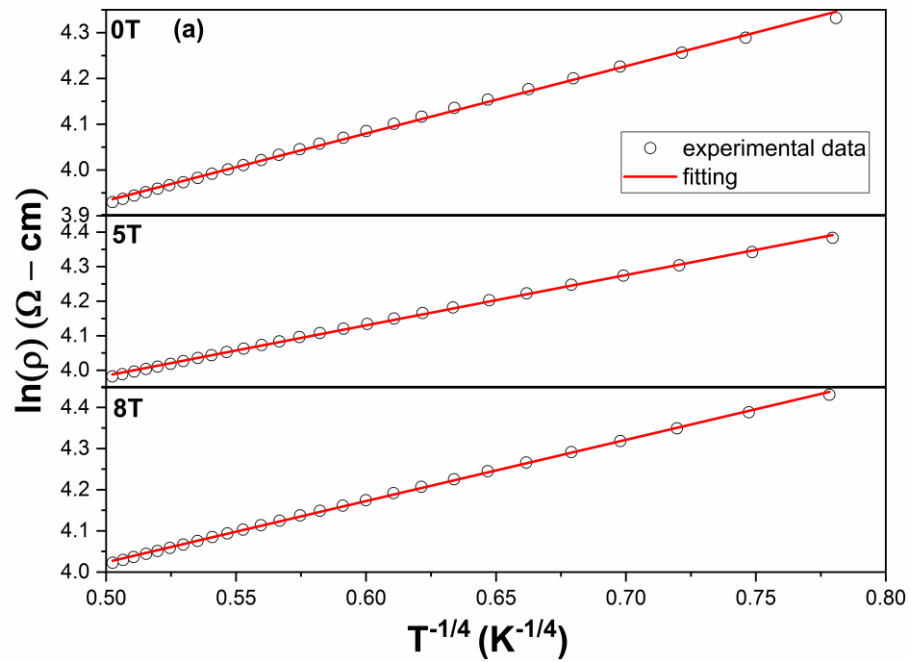
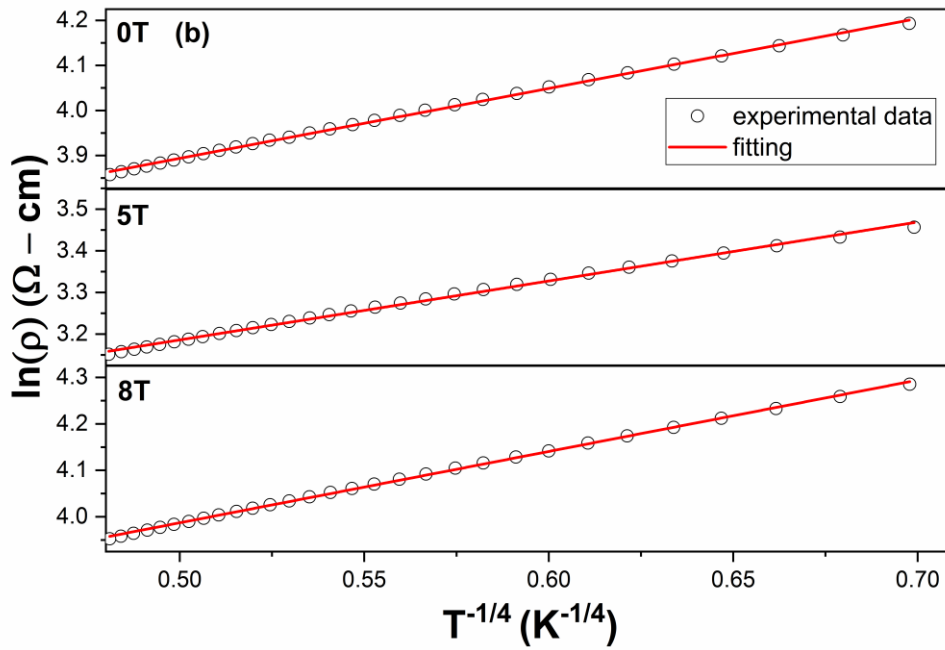
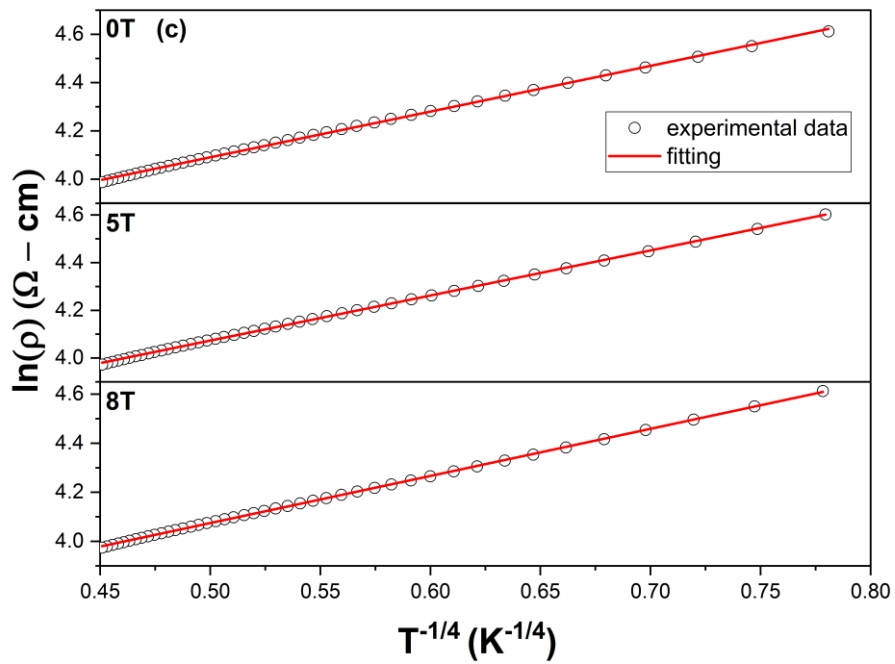


Figure 3.10(a): Fitting of VRH model in the temperature region 2 K – 25 K of  $x = 0$  sample.



*Figure 3.10(b): Fitting of VRH model in the temperature region 2 K – 25 K of  $x = 0.01$  sample.*



*Figure 3.10(c): Fitting of VRH model in the temperature region 2 K – 25 K of  $x = 0.03$  sample.*

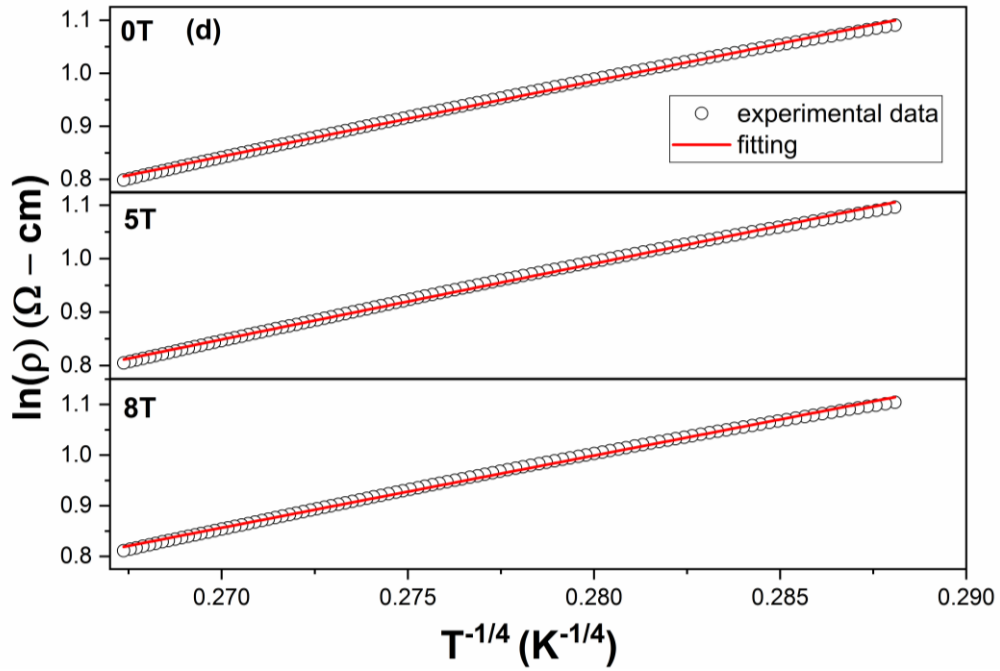


Figure 3.10(d): Fitting of VRH model in the temperature region 145 K – 195 K of  $x = 0.05$  sample.

Table 3.4: Values of Mott's temperature ( $T_0$ ) in the corresponding temperature ranges.

Applied Magnetic Field	$T_0$ (K) $\times 10^5$ (150 K – 255 K)			$T_0$ (K) $\times 10^4$ (145 K – 195 K)	$T_0$ (K) (2 K – 25 K)		
	$x = 0$	$x = 0.01$	$x = 0.03$	$x = 0.05$	$x = 0$	$x = 0.01$	$x = 0.03$
0T	1.863	1.376	4.401	6.032	7.163	6.521	15.556
5T	1.843	1.281	4.238	4.497	6.819	5.817	15.276
8T	1.826	1.077	4.193	4.141	6.439	5.566	14.909

### 3.3.4 Magnetotransport Studies

Magnetoresistance refers to change in the resistance of a material with respect to magnetic field. A magnetic material may experience localized spin fluctuations as a result of the application of a magnetic field. These fluctuations in localized spins lead to magnetic scattering, which in turn causes

magnetoresistance [43]. For a particular value of temperature, MR% can be evaluated using the equation-

$$M(R)\% = \frac{\rho(H,T) - \rho(0,T)}{\rho(0,T)} \times 100 \quad (3.7)$$

$\rho(H, T)$  and  $\rho(0, T)$  are resistivity values at magnetic field of H and zero respectively at a given temperature T. The measurement of the samples were carried out at a range of temperatures 5, 10, 15, 25, 50 and 100 K using Physical Property Measurement System (PPMS). The MR curves are displayed in Fig. 3.11(a-d). A negative trend of MR% is observed at low temperatures from 5 K – 50 K and the curve crosses over to the positive side at 100 K. In order to examine the dc magnetoresistivity, forward interference model and wave shrinkage model are typically employed.

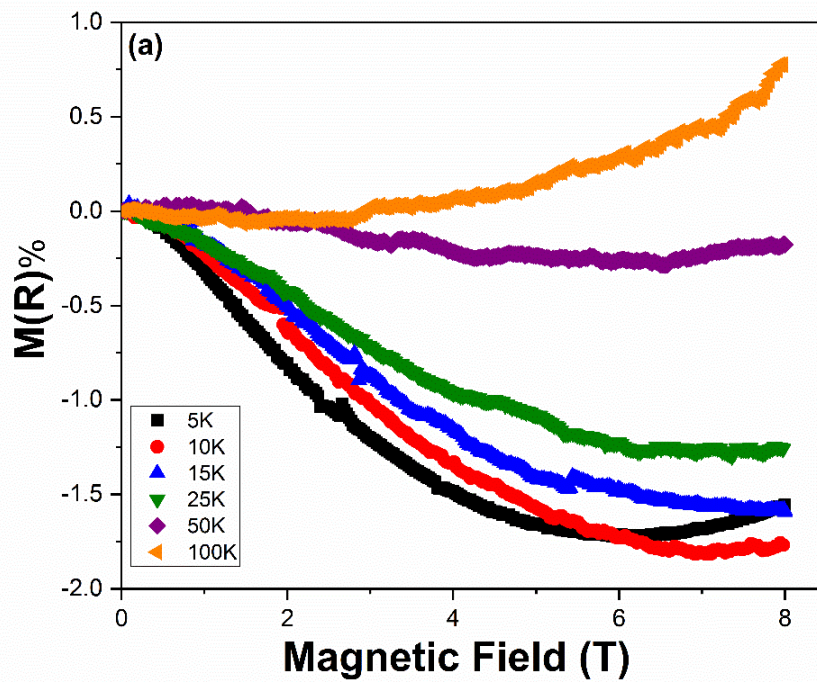


**Figure 3.11(a):** Magnetoresistance plot of  $Fe_{0.05}(Te)_{1-x}Sb_x$  bulk alloy for  $x = 0$  sample.

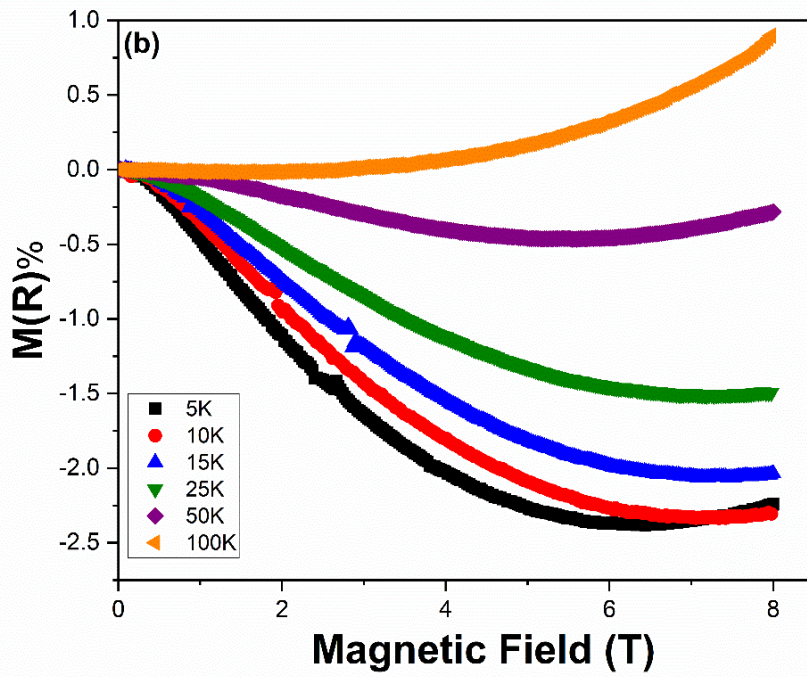


Figure 3.11(b): Magnetoconductance plot of  $Fe_{0.05}(Te)_{1-x}Sb_x$  bulk alloy for  $x = 0.01$  sample.

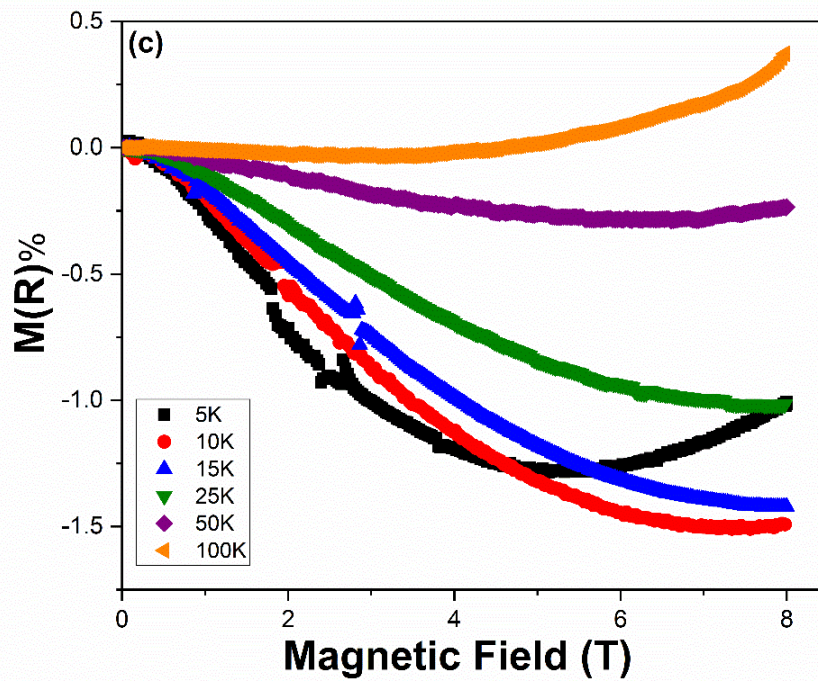
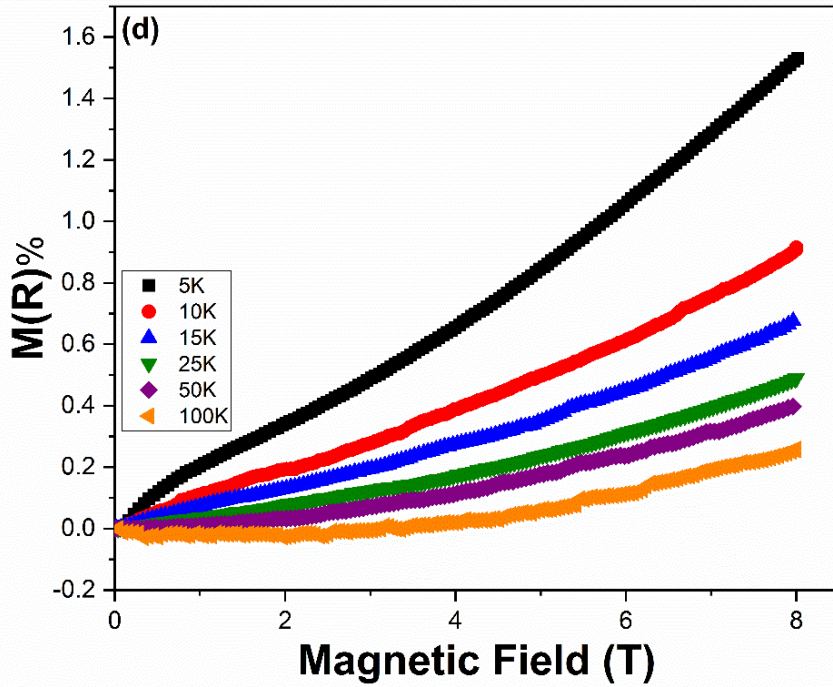


Figure 3.11(c): Magnetoconductance plot of  $Fe_{0.05}(Te)_{1-x}Sb_x$  bulk alloy for  $x = 0.03$  sample.



**Figure 3.11(d):** Magnetoresistance plot of  $Fe_{0.05}(Te)_{1-x}Sb_x$  bulk alloy for  $x = 0.05$  sample.

In forward interference model, there could be various path for electrons to hop from one site to another. The neighbouring sites are separated by a distance equal to optimum hopping distance. There is an interference among all these different paths between the hopping sites that causes the electrons to localize. Presence of magnetic field suppresses the destructive interference term which in turn leads to a decrease in the resistance, thereby enhancing the hopping mechanism. This mechanism seems to be the reason for the negative MR that is observed in  $x = 0, 0.01$  and  $0.03$  samples from  $5\text{ K} - 50\text{ K}$  [44]. On the other hand, in wave shrinkage model, a contraction in the wave function of localized electrons as well as that of the neighbouring site takes place. This reduces the overlap between these two wave functions which in turn reduces the hopping probability. The localization length decreases thereby increasing the resistance leading to a positive MR [45]. Positive MR is observed for  $x = 0, 0.01$  and  $0.03$  samples as the temperature is increased to  $100\text{ K}$ . However, in the case of  $x =$

0.05 sample, MR% is positive at all temperatures suggesting an increased localization.

### 3.3.5 Magnetic Studies

DC magnetization study of  $\text{Fe}_{0.05}(\text{Te})_{1-x}\text{Sb}_x$  samples ( $x = 0, 0.01, 0.03$  and  $0.05$ ) are performed using super conducting quantum interface device – vibrating sample magnetometer (SQUID-VSM) system for temperatures ranging from 10 K – 300 K. Measurements of magnetic moment v/s temperature (M-T) are made in both field cooling (FC) and zero field cooling (ZFC) settings. The samples are initially cooled in ZFC condition till 10 K followed by an application of an external magnetic field of 100 Oe while heating the samples till 300 K. However, in FC condition, cooling of sample already takes place in the presence of magnetic field of 100 Oe till 10 K. And once again, the sample is heated till 300 K in the presence of this magnetic field alongside noting the magnetic moment variation with temperature. The plots are represented by ZFC-FC curves as shown in Fig. 3.12(a-d).

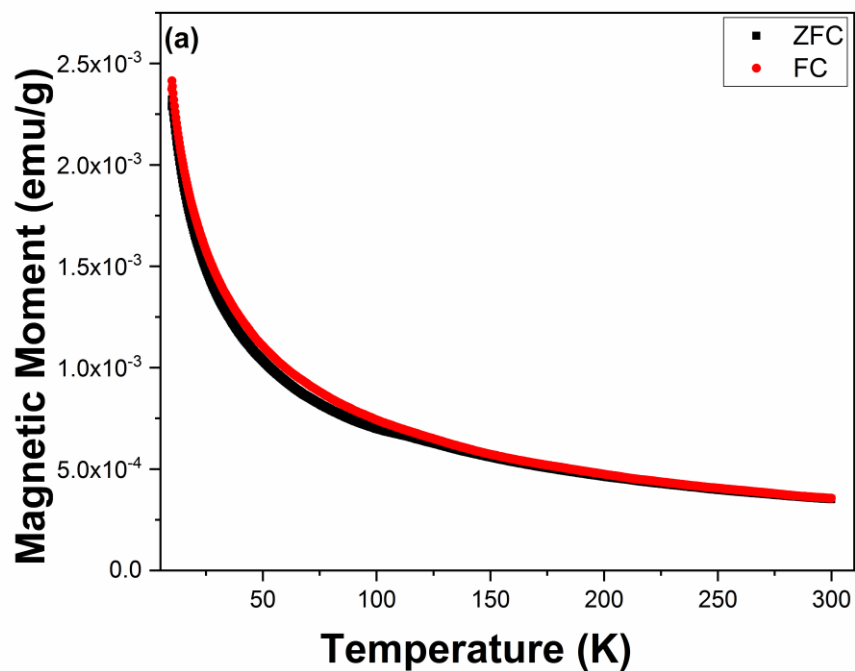


Figure 3.12(a): Magnetization vs Temperature plot under ZFC-FC condition for  $x = 0$  sample.

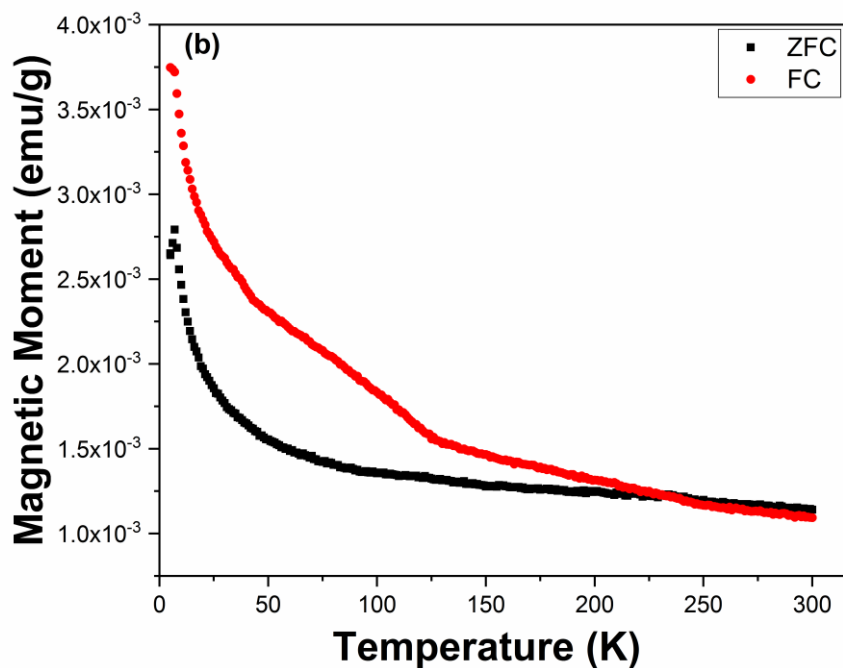


Figure 3.12(b): Magnetization vs Temperature plot under ZFC-FC condition for  $x = 0.01$  sample.

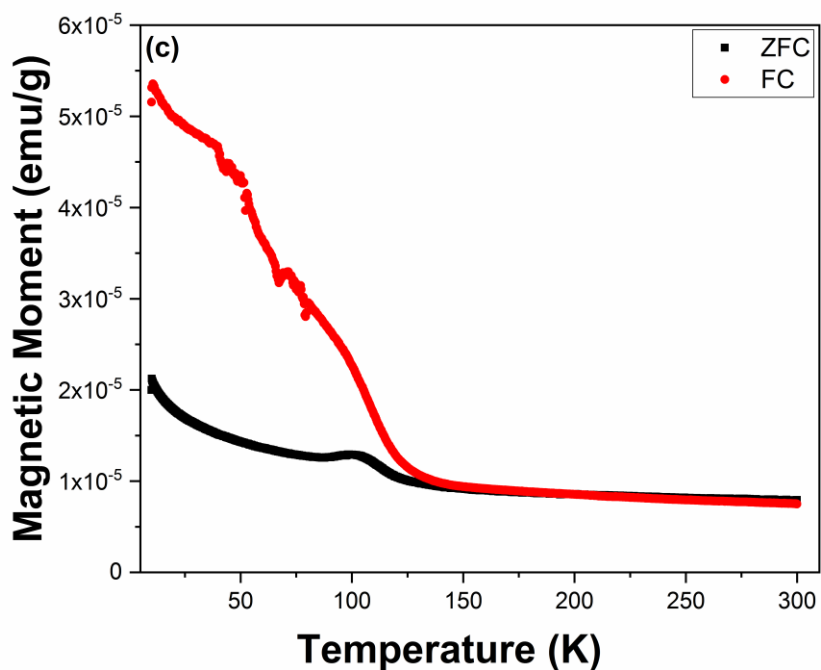
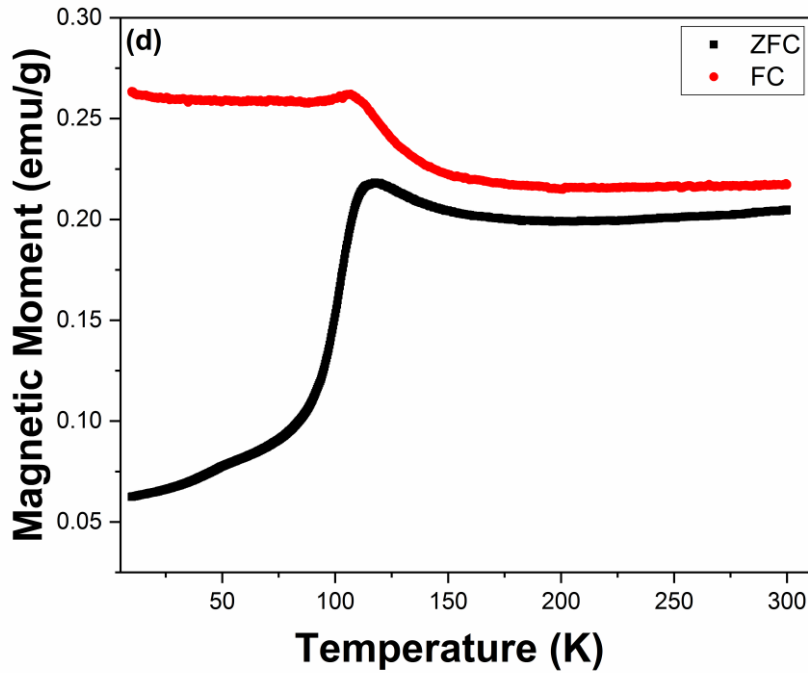


Figure 3.12(c): Magnetization vs Temperature plot under ZFC-FC condition for  $x = 0.03$  sample.



*Figure 3.12(d): Magnetization vs Temperature plot under ZFC-FC condition for  $x = 0.05$  sample.*

The plot of  $x = 0$  sample shows an overlap between both ZFC and FC curves at all values of temperature suggesting that only a single magnetic phase exists in the sample which corresponds to paramagnetism. It is known that pure Te is diamagnetic in nature [46]. Thus, doping with Fe brings about a change in its magnetic ordering i.e. from diamagnetism to paramagnetism.  $x = 0.01$  and  $0.03$  samples are also seen to exhibit paramagnetism at higher temperatures, but they are conspicuous by the absence of overlapping between the curves at lower values of temperature. The ZFC and FC curves of  $x = 0.01$  sample is seen to undergo a sharp upward trend with decreasing temperature whereas those of  $x = 0.03$  sample reveal a rising magnetization below 150 K. The samples thus seem to have a tendency of ferromagnetic ordering. There is also an inflection point observed in the ZFC curve of  $x = 0.03$  sample around 100 K that suggests an antiferromagnetic ordering. From the ZFC and FC curves of  $x = 0.05$  sample, there is no signature of paramagnetic property. A cusp that is present in both ZFC and FC curve corresponds to an antiferromagnetic phase of Fe-Sb [47]. In

addition, a large bifurcation is also observed between the ZFC and FC curves below the inflection point. Although, FC curve is found to be saturated at a constant value which is expected for a ferromagnetic transition, ZFC curve undergoes a considerable decrease in magnetization. There can be an occurrence of freezing of spins at such low values of temperature.

As paramagnetic ordering can only be seen from the ZFC-FC curves of  $x = 0, 0.01$  and  $0.03$  samples and not in  $x = 0.05$  sample, further exploration of its magnetic properties is carried out by plotting inverse susceptibility data as a function of temperature. However, Curie's law is unable to perfectly fit the  $\chi^{-1}(T)$  data of  $x = 0$  sample thereby making use of Curie-Weiss law which is defined as  $\chi = C / (T - \theta)$  where  $C$  denotes Curie constant and  $\theta$  denotes Curie – Weiss temperature. From Fig. 3.13(a), the entire curve is seen to follow Curie-Weiss law except at for the deviation at low temperature. From the fit, the values of parameters deduced are  $C = 1.27 \times 10^{-3}$  and  $\theta = -65.98$  and this negative value of  $\theta$  is what recognizes presence of an emerging antiferromagnetic property in the sample. Further, in both  $x = 0.01$  and  $0.03$  samples, the  $\chi^{-1}(T)$  plot as seen in Fig. 3.13(b) and (c) shows a linearity only in the high temperature region where on fitting with Curie-Weiss law, the value of  $\theta$  obtained is  $-269.88$  and  $-470.56$  respectively. The Curie-Weiss law is observed to be violated below  $140$  K of  $x = 0.03$  sample, as shown by a change in the slope of the inverse susceptibility curve. This points towards the presence of ferromagnetic order having short range in the system [48].

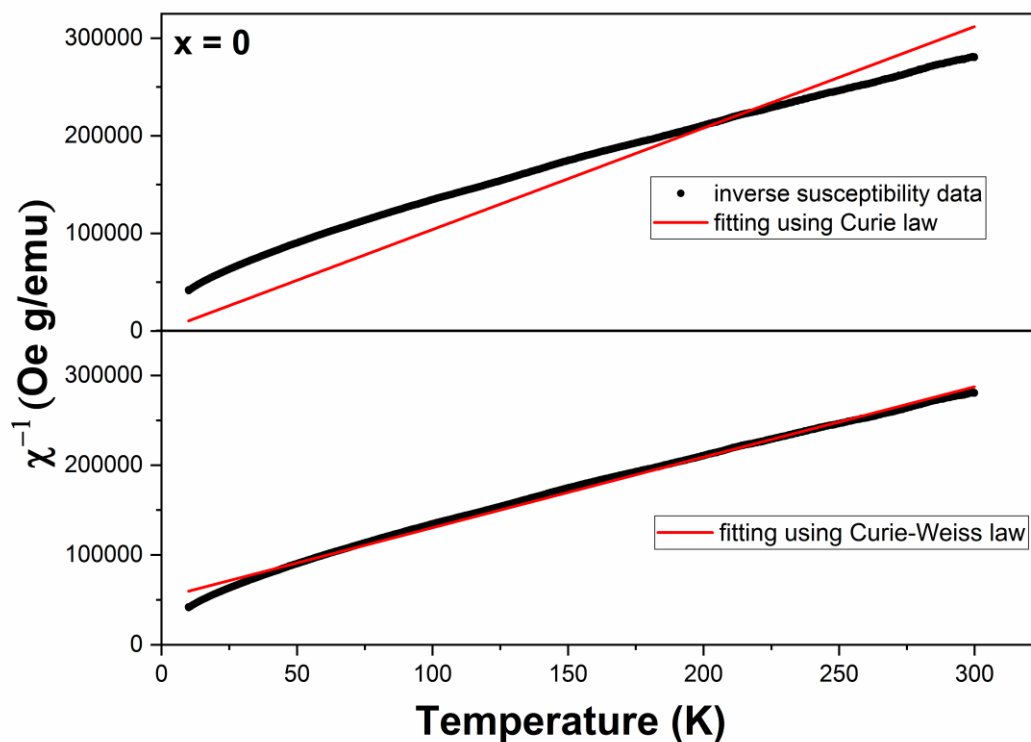


Figure 3.13(a): Inverse Susceptibility plot fitted using Curie and Curie-Weiss law as shown by red line for  $x = 0$  sample.

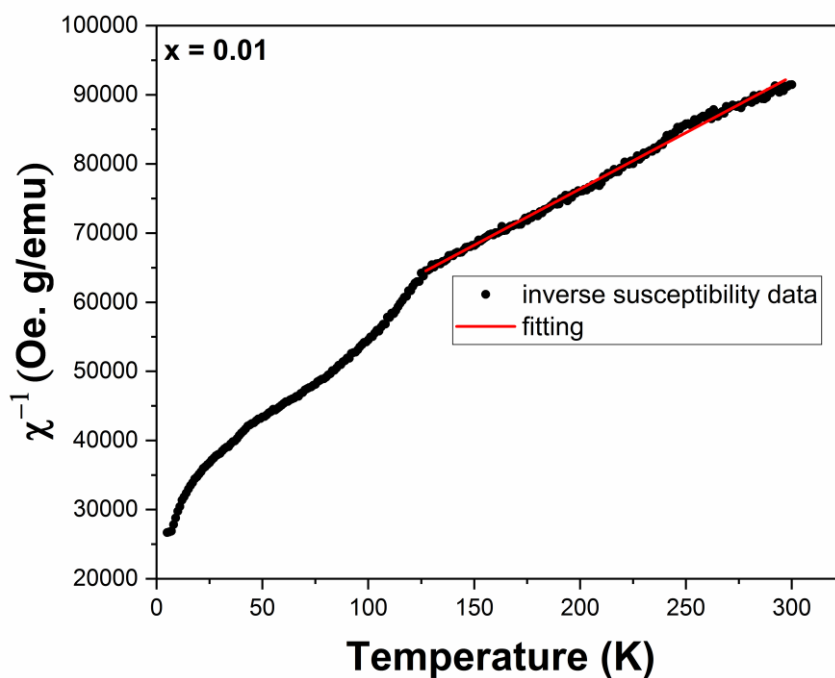
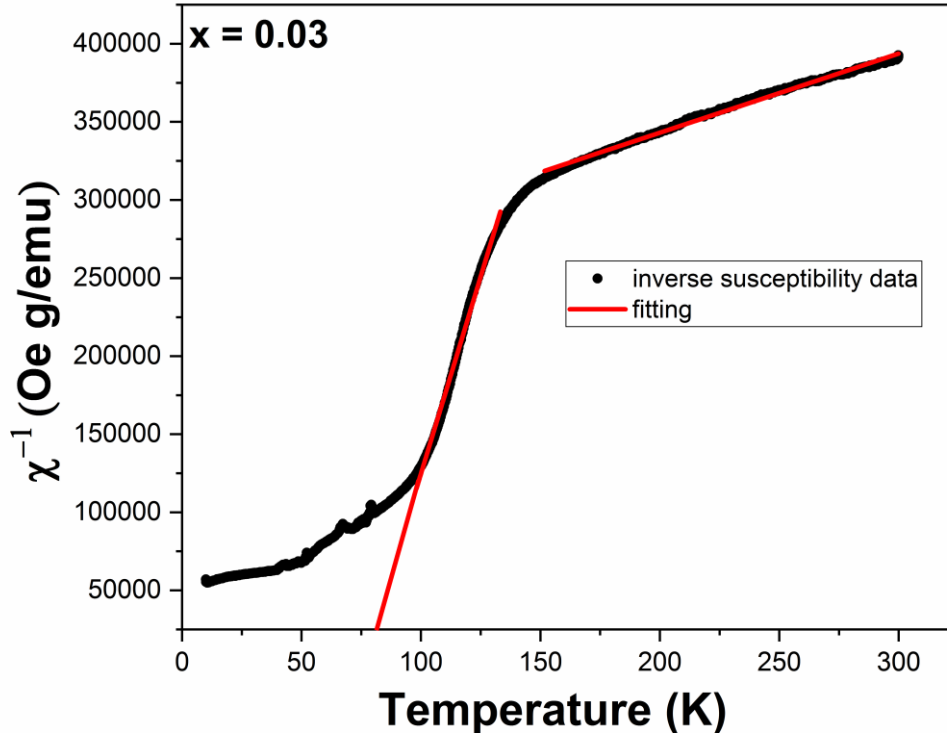


Figure 3.13(b): Inverse Susceptibility plot fitted using Curie-Weiss law (red line) for  $x = 0.01$  sample.



*Figure 3.13(c): Inverse Susceptibility plot fitted using Curie-Weiss law (red line) for  $x = 0.03$  sample.*

Magnetic hysteresis measurements are also performed to further investigate the magnetic characteristics of the samples at temperatures 100 K and 300 K up to an external magnetic field of 8 T. The M-H curve of  $x = 0$  sample as seen in Fig. 3.14(a) shows only paramagnetic ordering at both values of temperature. The magnetization curve is then fitted using the Langevin function which is important in the theory of paramagnetism and is expressed as

$$M(H) = n\mu L\left(\frac{\mu_0\mu H}{k_B T}\right) \text{ with } L(x) = \coth(x) - 1/x \quad (3.8)$$

$n$ ,  $\mu$ ,  $\mu_0$ ,  $k_B$  and  $T$  represent the density of magnetic cluster, average value of magnetic moment per cluster, permeability of vacuum, Boltzmann constant and absolute temperature respectively.

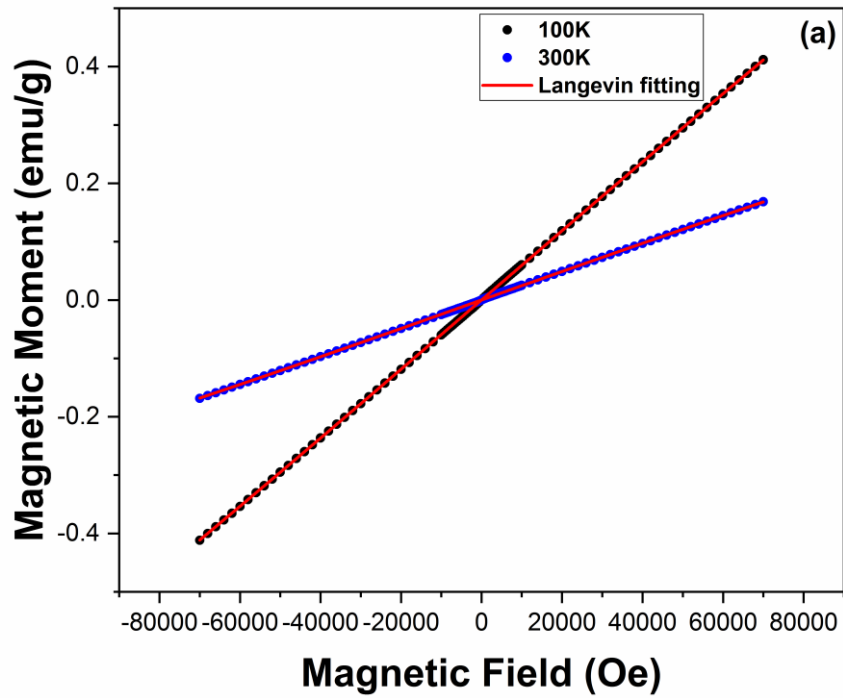


Figure 3.14(a):  $M$ - $H$  plot of  $Fe_{0.05}(Te)_{1-x}Sb_x$  bulk alloy for  $x = 0$  at 100 K and 300 K. Red line represents fitting using Langevin function.

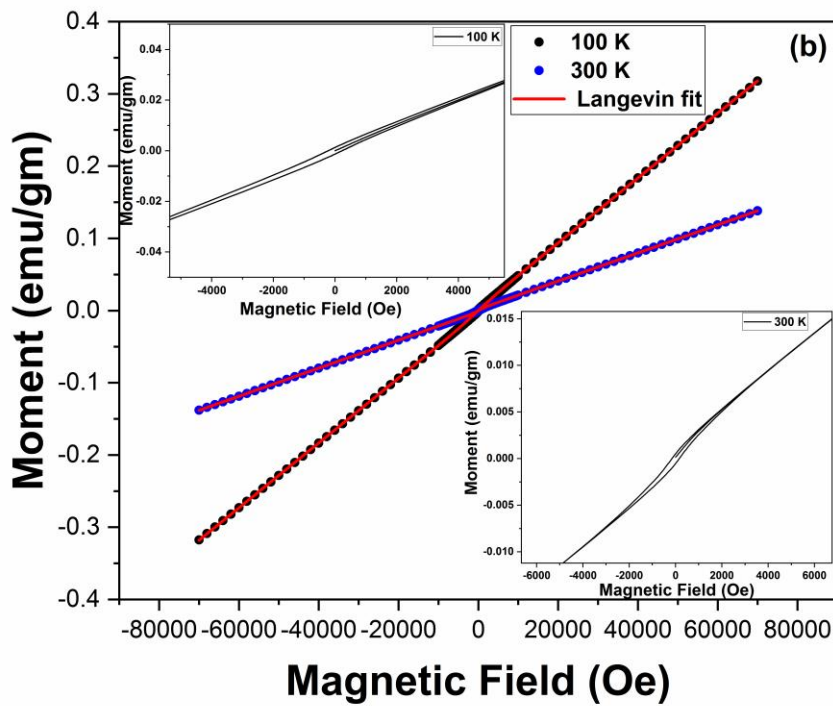
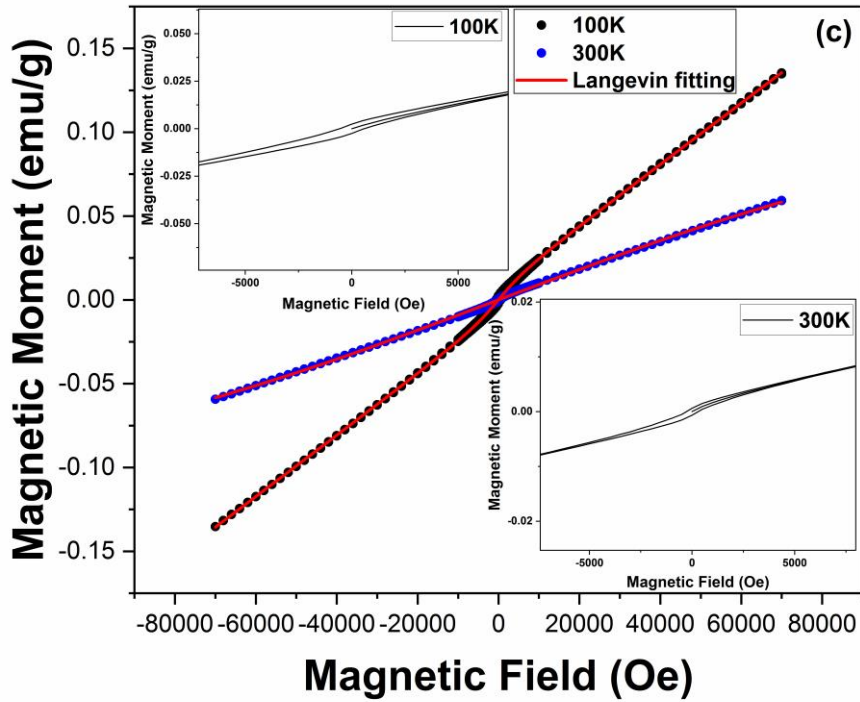


Figure 3.14(b):  $M$ - $H$  plot of  $Fe_{0.05}(Te)_{1-x}Sb_x$  bulk alloy for  $x = 0.01$  at 100 K and 300 K. Red line represents fitting using modified Langevin function.



**Figure 3.14(c):** *M-H plot of  $Fe_{0.05}(Te)_{1-x}Sb_x$  bulk alloy for  $x = 0.03$  at 100 K and 300 K. Red line represents fitting using Langevin function.*

However, in the M-H curves of  $x = 0.01$  and  $0.03$  sample as seen in Fig. 3.14(b) and (c), a small hysteresis loop can be observed which is an indication of a weak ferromagnetic behaviour having a small domain size. The hysteresis curve is smaller in case of  $x = 0.01$  sample having a coercivity value of 238 Oe at 100 K and 135 Oe at 300 K whereas for  $x = 0.03$  sample, it is enhanced, and the values are 605 Oe at 100 K and 220 Oe at 300 K. Another feature observed in the M(H) curve is presence of a linear behaviour at higher field values which depicts that the paramagnetic or antiferromagnetic feature still exists in these samples in addition to weak ferromagnetism. The M-H curves could not be fitted perfectly using the Langevin function defined above. Therefore, a modified Langevin function described below is adopted that is found to give a perfect fit to the curve.

$$M(H) = n\mu L\left(\frac{\mu_0\mu H}{k_B T}\right) + \chi H \quad (3.9)$$

An additional term  $\chi H$  has been introduced into the Langevin equation in order to approximate linear magnetization responses as a function of applied field.

Modified Langevin function is mainly applicable for weakly ferromagnetic samples that have super-paramagnetic domains. Nonetheless the same function was found to not fit the M-H curve at 300 K of  $x = 0.03$  sample but otherwise was best fitted using the Langevin function. The values of parameters that the fit yielded for  $x = 0.03$  sample are  $\mu = 5.54 \times 10^{-2} \mu_B$  and  $n = 1.65 \times 10^{21}/g$  for 100 K and  $\mu = 7.72 \times 10^{-3} \mu_B$  and  $n = 2.21 \times 10^{24}/g$  for 300 K. An increase in the value of  $n$  obtained from the fitting at 300 K implies a reduction in the domain size.

Therefore, with the substitution of Sb into the system, an improvement in the magnetic ordering is witnessed because of magnetic phase transition that has taken place. Sb that acts as a hole impurity in Te has led to an increase in the number of holes and this increase created a disparity in the amount of ‘up’ and ‘down’ spins thus aiding the system in giving rise to signals of weak ferromagnetism [49].

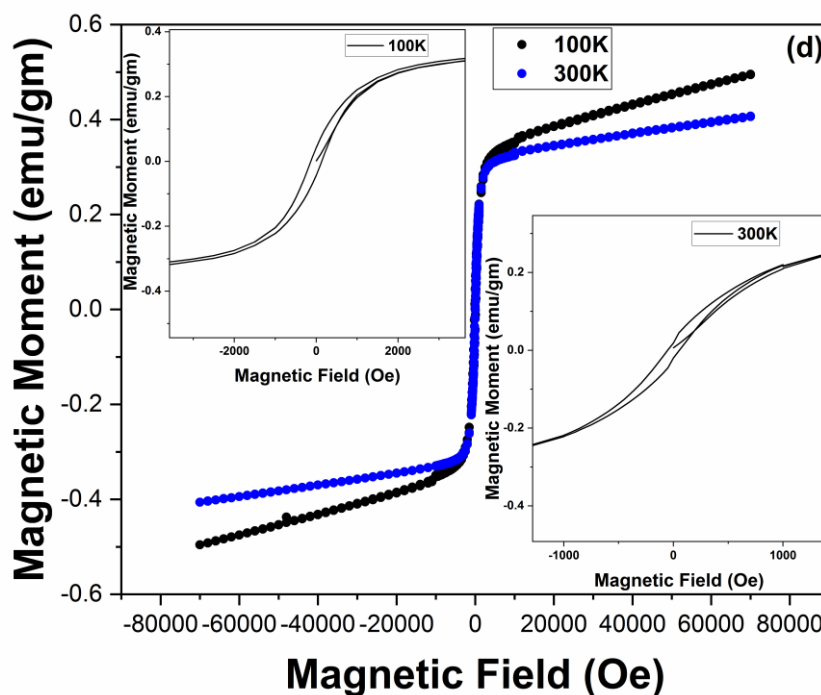


**Figure 3.14(d):** M-H plot of  $Fe_{0.05}(Te)_{1-x}Sb_x$  bulk alloy for  $x = 0.05$  at 100 K and 300 K.

On further increasing the concentration of Sb to  $x = 0.05$ , the M-H curve does not show any saturation at both temperatures as seen in Fig. 3.14(d). There

is however a presence of hysteresis albeit the value of coercivity which is extremely small as compared to that of  $x = 0.03$  sample i.e. 136 Oe at 100 K and 45 Oe at 300 K. Since the coercivity value undergoes suppression at room temperature, this accounts to presence of antiferromagnetic features in the sample. The presence of antiferromagnetic ordering is also evident from the inflection point in ZFC-FC curve of the sample.

## References

1. L. A. Ba, M. Doring, V. Jamier and C. Jacob, "Tellurium: an element with great biological potency and potential," *Org. Biomol. Chem.*, vol. 8, 4203 (2010).
2. A. P. Li and J. Shen, "Ferromagnetic percolation in  $Mn_xGe_{1-x}$  dilute magnetic semiconductor," *App. Phys. Lett.*, vol. 86, 152507 (2005).
3. N. Agrawal, M. Sarkar, M. Chawda and V. Ganesan, "Carrier induced magnetism in dilute Fe doped  $Ge_{1-x}Sb_x$  thin films," *Mat. Chem and Phys.*, vol. 143, 330 – 335 (2013).
4. D. R. S. Somayajulu, N. Patel, M. Chawda, M. Sarkar and K.C. Sebastian, "Concentration Dependence of Room Temperature Magnetic Ordering in Dilute Fe:  $Ge_{1-x}Te_x$  alloy," *Hyperfine Interactions*, vol. 160, 241 (2005).
5. N. Patel, M. Chawda, M. Sarkar, K. C. Sebastian, D. R. S. Somayajulu and A. Gupta, "Magnetic Ordering in  $Fe_{0.008}Ge_{1-x}D_x$  ( $D = As, Bi$ )," *Hyperfine Interactions*, vol. 160, 247 (2005).
6. R. Basnet et al., "Growth and Strain Engineering of Trigonal Te for Topological Quantum Phases in Non-Symmorphic Chiral Crystals," *Crystals*, vol. 9, 486 (2019).
7. H. J. Goldsmid, "Thermoelectric Refrigeration," Plenum Press, New York, 1964.
8. J. W. Liu, J. H. Zhu, C. L. Zhang, H. W. Liang and S. H. Yu, "Mesostructured Assemblies of Ultrathin Superlong Tellurium Nanowires and their Photoconductivity," *J. AM. Chem. Soc.*, vol. 132, 8945 (2010).
9. H. Tao, H. Liu, D. Qin, K. Chan, J. Chen and Y. Cao, "High mobility field effect transistor from solution-processed needle-like tellurium nanowires," *J. Nanosci. Nanotechnol.*, vol. 10, 7997 (2010).
10. L. A. Agapito, N. Kioussis, W. A. Goddard and N. P. Ong, "Novel Family of Chiral-Based Topological Insulators: Elemental Tellurium under Strain," *Phys. Rev. Lett.*, vol. 110, 176401 (2013).

11. T. Engelhard, E. Jones, L. Viney, Y. Mastai and G. Hodes, "Deposition of tellurium films by decomposition of electrochemically-generated  $H_2Te$ : Application to radiative cooling devices," *Thin Solid Films*, vol. 370, 101 (2000).
12. V. M. Asnin, A. A. Bakun, A. M. Danishevskii, E. L. Ivchenko, G. E. Pikus and A. A. Rogachev, "Circular photogalvanic effect in optically active crystals," *Solid State Commun.*, vol. 30, 565 (1979).
13. T. I. Lee et al., "High-power density piezoelectric energy harvesting using radially strained ultrathin trigonal tellurium nanowire assembly," *Adv Mater.*, vol. 25, 2920 (2013).
14. J. Chen, Y. Dai, Y. Ma, X. Dai, W. Ho and M. Xie, "Ultrathin  $\beta$ -tellurium layers grown on highly oriented pyrolytic graphite by molecular-beam epitaxy," *Nanoscale*, vol. 24, 15945 (2017).
15. C. D. Brown, D. M. Cruz, A. K. Roy and T. J. Webster, "Synthesis and characterization of PVP-coated tellurium nanorods and their antibacterial and anticancer properties," *J. Nanoparticle Res.*, vol. 20, 254 (2018).
16. S. Tutihasi, G. G. Roberts, R. C. Keezer and R. E. Drews, "Optical properties of tellurium in the fundamental absorption region," *Phys. Rev.*, vol. 177, 1143 (1969).
17. L. Han et al., "Visible nonlinear optical properties of tellurium and application as saturable absorber," *Opt. Laser Technol.*, vol. 137, 106817 (2021).
18. G. Qiu, A. Charnas, C. Niu, Y. Wang, W. Wu and P. D. Ye, "The resurrection of tellurium as an elemental two-dimensional semiconductor," *npj 2D Mater Appl.*, vol. 6, 17 (2022).
19. T. Zhu, Y. Zhang, X. Wei, M. Jiang and H. Xu, "The rise of two-dimensional tellurium for next-generation electronics and optoelectronics," *Front. Phys.*, vol. 18, 33601 (2023).

20. S. Lin, W. Li, Z.Chen, J. Shen, B. Ge and Y. Pei, “Tellurium as a high-performance elemental thermoelectric,” *Nat. Commun.*, vol. 7, 10287 (2016).
21. K. Akiba, K. Kobayashi, T. C. Kobayashi, R. Koezuka, A. Miyake, J. Gouchi, Y. Uwatoko and M. Tokunaga, “Magnetotransport properties of tellurium under extreme conditions,” *Phy. Rev. B*, vol. 101, 245111 (2020).
22. T. Ideue et al., “Pressure-induced topological phase transition in noncentrosymmetric elemental tellurium,” *Proc. Natl. Acad. Sci. U.S.A.*, vol. 116, 25530 (2019).
23. J. F. Oliveira et al., “Pressure-induced Anderson-Mott transition in elemental tellurium,” *Commun. Mater.*, vol. 2, 1 (2021).
24. M. Hirayama, R. Okugawa, S. Ishibashi, S. Murakami and T. Miyake, “Weyl Node and Spin Texture in Trigonal Tellurium and Selenium,” *Phys. Rev. Lett.*, vol. 114, 206401 (2015).
25. N. Zhang, B. Cheng, H. Li, L. Li and C. G. Zeng, “Magneto-transport properties of thin flakes of Weyl semiconductor tellurium,” *Chin. Phys. B*, vol. 30, 087304 (2021).
26. Y. Ji et al., “Quantum Linear Magnetoresistance and Nontrivial Berry Phase in High-Mobility Elemental Tellurium,” *Ad. Electron. Mater.*, vol. 8, 2200654 (2022).
27. P. K. Mishra, P. D. Babu, G. Ravikumar, R. Mishra, M. Roy, S. Phapale and P. U. Sastry, “Possible room temperature ferromagnetism in silicon doped tellurium semiconductor,” *J. Alloys Compd.*, vol. 639, 5 (2015).
28. T. Furukawa, Y. Shimokawa, K. Kobayashi and T. Itou, “Observation of current-induced bulk magnetization in elemental tellurium,” *Nat. Commun.*, vol. 8, 954 (2017).

29. F. Sun et al., "Hole doping and pressure effects on the II-II-V based diluted magnetic semiconductor  $(\text{Ba}_{1-x}\text{K}_x)(\text{Zn}_{1-y}\text{Mn}_y)_2\text{As}_2$ ," *Phys. Rev. B*, vol. 95, 094412 (2017).
30. C. Suryanarayana, M. G. Norton, *Crystal Structure Determination. II: Hexagonal Structures*. In: *X-Ray Diffraction*. Springer, Boston, MA, 1998, 97-123.
31. D. Balzar and H. Ledbetter, "Voigt-function modeling in Fourier analysis of size- and strain- broadened X-ray diffraction peaks," *J. Appl. Cryst.*, vol. 26, 97 (1993).
32. G. Carotenuto, M. Palomba, S.D. Nicola, G. Ambrosone, U. Coscia, "Structural and Photoconductivity Properties of Tellurium/PMMA Films," *Nanoscale Res. Lett.*, vol. 10, 313 (2015).
33. D.K. Sang, B. Wen, S. Gao, Y. Zeng, F. Meng, Z. Guo and H. Zhang, "Electronic and Optical Properties of Two-Dimensional Tellurene: From First-Principles Calculation," *Nanomaterials*, vol. 9, 1075 (2019).
34. H. Zhang, J. Wang, F. Guégan, S. Yu and G. Frapper, "Prediction of allotropes of tellurium with molecular, one- and two- dimensional covalent nets for photofunctional applications," *RSC Adv.*, vol. 11, 29965 (2021).
35. J. Kurian and R. Singh, "Electron spin resonance and resistivity studies of charge-ordered  $\text{Bi}_{1-x}\text{Ca}_x\text{MnO}_3$ ," *J. Phys. D: Appl. Phys.*, vol. 41, 215006 (2008).
36. N. S. Bennett, "Thermoelectric performance in n-type bulk silicon: The influence of dopant concentration and dopant species," *Phys. Status Solidi A*, vol. 214, 1700307 (2017).
37. A. G. Zabrodskii and K. N. Zinov'eva, "Low temperature conductivity and metal-insulator transition in compensate n-Ge," *Sov. Phys. JETP*, vol. 52, 2 (1984).

38. Z. W. Fan, P. Li, E. Y. Jiang and H. L. Bai, "Evolution of magnetoresistance mechanisms in granular Co/C films with different conduction regimes," *J. Phys. D: Appl. Phys.*, vol. 46, 065002 (2013).
39. S. Sagar and M. R. Anantharaman, "On conduction mechanism in paramagnetic phase of Gd based manganites," *Bull. Mater. Sci.*, vol. 35, 41(2012).
40. G. Lalitha and P. Venugopal Reddy, "Low temperature resistivity anomalies in bismuth doped manganites," *J. Alloys Compd.*, vol. 494, 476 (2010).
41. V. Ambegaokar, B. I. Halperin and J. S. Langer, "Hopping Conductivity in Disordered Systems," *Phys. Rev. B*, vol. 4, 2612 (1971).
42. Y. Sun, X. Xu and Y. Zhang, "Variable-Range Hopping of Small Polarons in Mixed-Valence Manganites," *J. Phys. Condens. Matter.*, vol. 12, 10475 (2000).
43. S. Chatterjee, R. Maiti and D. Chakravorty, "Large magnetodielectric effect and negative magnetoresistance in NiO nanoparticles at room temperature," *RSC Adv.*, vol. 10, 13708 (2020).
44. J. Guo, *et al*, "Enhanced Negative Magnetoresistance with High Sensitivity of Polyaniline Interfaced with Nanotitania," *J. Electrochem. Soc.*, vol. 163, H664 (2016).
45. C. Majumder, S. Bhattacharya, T. K. Mondal and S. K. Saha, "Ferromagnetism with high magnetoresistance in Ag decorated graphitic carbon nitride," *J. Magn. Magn. Mater.*, vol. 535, 167941 (2021).
46. S. R. Rao and S. R. Govindarajan, "The crystal diamagnetism of tellurium," *Proc. Indian Acad. Sci.*, vol. 10, 235 (1939).
47. P. J. Picone and P. E. Clark, "Mössbauer measurements on lattice and interstitial iron atoms in  $\text{Fe}_{1+x}\text{Sb}$  alloys," *J. Magn. Magn. Mater.*, vol. 12, 233 (1979).

48. R. Kamel, A. Tozri, E. Dhahri and E. K. Hlil, “Anomalous behaviour above the Curie temperature in  $(\text{Nd}_{1-x}\text{Gd}_x)_{0.55}\text{Sr}_{0.45}\text{MnO}_3$  ( $x = 0, 0.1, 0.3$  and  $0.5$ ),” RSC Adv., vol. 9, 27541 (2019).
49. A. Zunger, S. Lany and H. Raebiger, “The quest for dilute ferromagnetism in semiconductors: Guides and misguides by theory,” Physics, vol. 3, 53 (2010).